Author/s:
Montoya Duque, E;Huang, Y;Siems, ST;May, PT;Protat, A;McFarquhar, GM

Title:
A Characterization of Clouds and Precipitation Over the Southern Ocean From Synoptic to Micro Scales During the CAPRICORN Field Campaigns

Date:
2022-09-16

Citation:
Montoya Duque, E., Huang, Y., Siems, S. T., May, P. T., Protat, A. & McFarquhar, G. M. (2022). A Characterization of Clouds and Precipitation Over the Southern Ocean From Synoptic to Micro Scales During the CAPRICORN Field Campaigns. Journal of Geophysical Research Atmospheres, 127 (17), https://doi.org/10.1029/2022JD036796.

ADVANCING EARTH AND SPACE SCIENCE

JGR Atmospheres

RESEARCH ARTICLE
10.1029/2022JD036796

**Special Section:**
Southern Ocean clouds, aerosols, precipitation and radiation

**Key Points:**

- Distinct cloud and precipitation regimes correspond to the Southern Ocean synoptics, defined using a sounding K-means clustering technique
- Evidence suggests diverse microphysical features, like mixed phase in shallow convection and ice aggregation in deep precipitating clouds
- Two unique synoptic patterns have unique cloud and precipitation properties over the high-latitudes, where climate models have large biases

**Correspondence to:**
E. Montoya Duque,
emontoyaduqu@student.unimelb.edu.au

**Citation:**
Montoya Duque, E., Huang, Y., Siems, S. T., May, P. T., Protat, A., & McFarquhar, G. M. (2022). A characterization of clouds and precipitation over the Southern Ocean from synoptic to micro scales during the CAPRICORN field campaigns. *Journal of Geophysical Research: Atmospheres*, *127*, e2022JD036796. https://doi.org/10.1029/2022JD036796

Received 18 MAR 2022
Accepted 23 JUL 2022

# A Characterization of Clouds and Precipitation Over the Southern Ocean From Synoptic to Micro Scales During the CAPRICORN Field Campaigns

**E. Montoya Duque[1,2], Y. Huang[1,2], S. T. Siems[2,3], P. T. May[3], A. Protat[4], and G. M. McFarquhar[5,6]**

[1]The University of Melbourne, Melbourne, VIC, Australia, [2]Australian Research Council Centre of Excellence for Climate Extremes, Melbourne, VIC, Australia, [3]Monash University, Melbourne, VIC, Australia, [4]Australian Bureau of Meteorology, Melbourne, VIC, Australia, [5]Cooperative Institute for Severe and High Impact Weather Research and Operations (CIWRO), University of Oklahoma, Norman, OK, USA, [6]School of Meteorology, University of Oklahoma, Norman, OK, USA

## Abstract

The persistent Southern Ocean (SO) shortwave radiation biases in climate models and reanalyses have been associated with the poor representation of clouds, precipitation, aerosols, the atmospheric boundary layer, and their intrinsic interactions. Capitalizing on shipborne observations collected during the Clouds Aerosols Precipitation Radiation and atmospheric Composition Over the Southern Ocean 2016 and 2018 field campaigns, this research investigates and characterizes cloud and precipitation processes from synoptic to micro scales. Distinct cloud and precipitation regimes are found to correspond to the seven thermodynamic clusters established using a K-means clustering technique, while less distinctions are evident using the cyclone and (cold) front compositing methods. Cloud radar and disdrometer data reveal that light precipitation is common over the SO with higher intensities associated with cyclonic and warm frontal regions. Multiple lines of evidence suggest the presence of diverse microphysical features in several cloud regimes, including the likely dominance of ice aggregation in deep precipitating clouds. Signatures of mixed phase, and in some cases, riming were detected in shallow convective clouds away from the frontal conditions. Two of the K-means clusters with contrasting cloud and precipitation properties are observed over the high-latitude SO and coastal Antarctica, suggesting distinct physical processes therein. Through a single case study, in-situ and remote-sensing data collected by an overflight of the Southern Ocean Clouds Radiation Aerosol Transport Experimental Study were also evaluated and complement the ship-based analysis.

## Plain Language Summary

The current generation of climate models and reanalyses products have difficulties in properly representing the radiative balance over the Southern Ocean (SO), which can be traced to the poor understanding of clouds and precipitation processes in this region. The remote location of the SO is a key factor for the lack of field observations that allow the scientific community to address the above-mentioned problem. However, recent coordinated field campaigns have collected an unprecedented amount of data, offering new opportunities to explore this understudied region. This research paper aims to study clouds and precipitation processes over the SO using shipborne data collected from two field campaigns in 2016 and 2018. Using different synoptic classification techniques, we identify unique macro and micro cloud and precipitation behaviors that correspond to the various weather patterns across a wide range of latitudes. In addition, we use aircraft observations collected from an overflight to evaluate and complement our analysis of the shipborne data. The study offers a framework that may help better understand the nature of the model biases over the SO.

## 1. Introduction

The Southern Ocean (SO) is a region of significant interest for its capacity to store excess heat and carbon. Yet large shortwave radiative biases over the SO continue to exist in both climate models and reanalysis products, which are primarily attributed to the poor representation of clouds, precipitation, aerosols, and their interactions in this region (Bodas-Salcedo et al., 2012, 2014; Kay et al., 2016; McFarquhar et al., 2021; Zelinka et al., 2020). These errors limit the ability of models to predict climate in this region, and the associated global climate feedbacks (Bodas-Salcedo et al., 2014; Ceppi et al., 2016; Gettelman et al., 2019).

While many studies have found that an incorrect ice-liquid partitioning, typically in the cold sector of extratropical cyclones (Bodas-Salcedo et al., 2012, 2014; Naud et al., 2014; Williams et al., 2013), constitutes a leading cause of the model biases, mechanisms that are responsible for these deficiencies are not yet clear. In addition, compensating errors associated with multi-layer clouds (Protat et al., 2017), biases in the frontal region of extratropical cyclones (Kelleher & Grise, 2019), as well as errors in shallow cyclones near the Antarctic continent (Mason et al., 2015) have all been documented. These findings underline the complicated nature of the models' biases and the dynamical and physical processes at play.

The challenges in understanding and modeling the SO climate have helped motivate a number of recent international field campaigns with the aim to improve the fundamental understanding of key atmospheric processes in this region through coordinated aircraft, shipborne and ground-based observations. Among these efforts, four recent collaborative field campaigns funded by agencies in the United States and Australia are summarized in McFarquhar et al. (2021). These projects include (a) The Clouds Aerosols Precipitation Radiation and atmospheric Composition Over the Southern Ocean (CAPRICORN), 2016 and 2018; (b) The Macquarie Island Cloud Radiation Experiment (MICRE), 2016–2018; (c) The Measurements of Aerosol, Radiation, and Clouds over the Southern Ocean (MARCUS), 2017–2018; (d) The Southern Ocean Cloud Radiation and Aerosol Transport Experimental Study (SOCRATES), 2018.

The comprehensive measurements collected from these projects are being utilized to examine clouds, aerosols, precipitation, and radiation characteristics over the SO in unprecedented detail. Using remote-sensing and in-situ observations, recent studies have refined our understanding of the bulk statistics of cloud occurrence and phase partitioning (Mace & Protat, 2018a), properties of non-precipitating liquid-phase low-level clouds (Mace & Protat, 2018b; Mace et al., 2021; Y. Wang et al., 2021), as well as cloud properties in the cold sector of extratropical cyclones (D'Alessandro et al., 2021; Y. Wang et al., 2020; Zaremba et al., 2020). Case studies have also been carried out to examine special phenomena such as an atmospheric river (Finlon et al., 2020), mesoscale cellular convection (Lang et al., 2021), and convective generating cells near the cloud tops (Alexander et al., 2021; Y. Wang et al., 2020). These new observations have also enabled the evaluation of model simulations across a range of spatial and temporal scales (Atlas et al., 2020; Gettelman et al., 2020; Protat et al., 2017; Zhou et al., 2020).

Despite the significant advancements, many key questions remain unaddressed. One understudied area is the understanding of processes involved in the life cycle of precipitation. Previous studies using precipitation records from Macquarie Island have identified the prevalence of drizzle and light precipitation and linked their bulk statistics to frontal and cyclonic activities (Lang et al., 2018; Z. Wang et al., 2015). More broadly, however, precipitation properties across the SO are largely unknown. Model errors in precipitation processes, such as the long-standing "warm-rain" process errors, remain widespread in the latest generation of climate models, which bias cloud feedbacks by as much as the CMIP5-to-CMIP6 climate sensitivity difference (Mülmenstädt et al., 2021).

Moreover, fewer studies have thus far focused on understanding the thermodynamic structure of the lower troposphere and how it controls the cloud-precipitation properties and processes over the SO, within the context of synoptic meteorology. Understanding these relationships is of importance, as the thermodynamics is arguably the largest term in water budget between different cloud types (McCoy et al., 2021). It is beneficial to explore these relationships at shorter timescales, given the transient nature of the weather systems that dominate the mid- and high-latitudes (Kelleher & Grise, 2019). Such practice is also a necessary step toward developing a physical, process-level understanding that is required for constraining the cloud-precipitation processes while mitigating compensating process errors in climate models (Mülmenstädt et al., 2021).

Using the collection of 2186 atmospheric soundings from the above-mentioned field campaigns, a recent study by Truong et al. (2020) was among the first to examine the relationships between the synoptic meteorology and lower tropospheric thermodynamic structure over the SO, using a K-means clustering complemented by front and cyclone composite analyses. The authors identified seven distinct clusters, which uniquely represent the various thermodynamic conditions over the SO, extending the knowledge derived from a 16-year record of soundings from Macquarie Island, where the midlatitude storm track clusters dominate (Lang et al., 2018).

The aim of this study is to examine cloud-precipitation properties and processes within the context of the thermodynamic clusters identified by Truong et al. (2020), as well as front and cyclone composites, using the shipborne observations collected from CAPRICORN experiments. In particular, we seek to address two questions: (a) Are there distinct cloud regimes that correspond to the unique thermodynamic and synoptic conditions? (b) How do the microphysical and precipitation processes differ in the various cloud regimes and atmospheric environments?

We also present a case study, where simultaneous remote-sensing and in-situ observations are available to provide further insights into the interplay between multiple processes. The description of the data and methods is presented in Section 2. Results are in Sections 3 and 4. Finally, the discussion and conclusions are in Section 5.

## 2. Data and Methods

### 2.1. Field Campaigns

The CAPRICORN field campaign was conducted with the Research Vessel (RV) Investigator, operated by the Australian Marine National Facility, consisting of two voyages led by the Australian Bureau of Meteorology (BoM). The first voyage (CAPRICORN I) was carried out from 13 March to 15 April 2016, traversing in the Australian water between Hobart, Australia (42.8°S, 147.3°E) and around 55°S. CAPRICORN II was executed in the austral summer (from 11 January to 21 February 2018) and had a broader latitudinal coverage (from Hobart to around 64°S). As the ship track was primarily designed to meet oceanographic objectives, the RV Investigator sometimes remained at the same station for 6–24 hr, commonly at high latitudes poleward of the oceanic polar front. Together these two voyages produce a rich data set encompassing clouds, aerosols, precipitation, and radiation measurements over the Australian sector of the SO (McFarquhar et al., 2021).

The Southern Ocean Cloud Radiation and Aerosol Transport Experimental Study (SOCRATES) campaign undertook 15 research flights from Hobart to near 62°S (134–163°E) during January–February of 2018 (McFarquhar et al., 2021). The flights were undertaken with the NSF/NCAR HIAPER Gulfstream V (GV) aircraft, making in-situ and airborne remote-sensing measurements of cloud, aerosol, and planetary boundary layer (PBL) properties, including (but not limited to) the structures and vertical distributions of liquid and mixed-phase clouds and aerosols. The flights were designed to sample the cold sectors of extratropical cyclones, where many climate models have the largest radiation biases (Marchand et al., 2014; McFarquhar et al., 2021). We make use of data collected from a flight coordinated over the ship on 23 January 2018.

### 2.2. Remote Sensing Data

Both the RV Investigator and the GV HIAPER included Doppler cloud radar (see Table 1), allowing for an opportunity to obtain synchronous cloud radar data during periods when the aircraft was close to the ship. As has been established in the literature (Bodas-Salcedo et al., 2011; Franklin et al., 2013; Haynes et al., 2009; Huang et al., 2015; Wood et al., 2009), a cloud radar detects different types of ice and water particles. For an in-cloud temperature less than 0°C, reflectivities larger than 5 dBZ commonly indicate a cloud dominated by large ice particles, and those less than 5 dBZ indicate Super-cooled Liquid Water (SLW) and/or small ice particles (including their coexistence) (Bodas-Salcedo et al., 2011). For temperatures greater than 0°C, liquid non-precipitating clouds are typically represented by a reflectivity lower than −15 dBZ, drizzle by radar reflectivities between −15 and −7.5 dBZ, and precipitating clouds by a reflectivity larger than −7.5 dBZ (Wood et al., 2009).

The cloud radar from the CAPRICORN/SOCRATES field campaigns also measured Doppler velocity, which is a combination of falling particles' speed and vertical wind speed when the cloud radar was vertically pointing. Different ice habits have distinct falling speeds, making it difficult to identify the type of ice with this instrument. Thus, it is not possible to quantify the presence of ice types, processes, or precipitation solely using cloud radar reflectivity, Doppler velocity and temperature (Mace & Protat, 2018a). Nevertheless, it is still possible to deduce the likely presence of certain shapes or sizes of ice particles on a qualitative level. We use the disdrometer to complement the analysis as well as in-situ measurements to evaluate a case study (Section 4).

### 2.3. In Situ Data

To measure surface precipitation, the RV Investigator employed an ODM470 disdrometer, which is part of the OceanRAIN data set (Ocean Rainfall And Ice-phase precipitation measurement Network, Klepp et al., 2018), see Table 1. Values below 0.01 mm/hr and spurious data are set to zero (refer to Klepp et al. (2018) for details on the intensity labeling). Note that the thermodynamic phase has inherent uncertainties in the estimated precipitation rates for mixed and snow phase precipitation (Klepp et al., 2018). Nevertheless, using the disdrometer allows us to have more information about the surface precipitation intensity and phase under different synoptic scenarios. Our initial analysis has identified two precipitation events with a 1-min precipitation rate apparently exceeding

**Table 1**

*Remote Sensors and In-Situ Instruments Deployed on the Research Vessel Investigator and Gulfstream V (HIAPER) Aircraft During the Clouds Aerosols Precipitation Radiation and Atmospheric Composition Over the Southern Ocean (CAPRICORN) and Southern Ocean Cloud Radiation and Aerosol Transport Experimental Study (SOCRATES) Field Campaigns*

| Instrument name | Description | Measurement ranges | Key variables | Uncertainties |
|---|---|---|---|---|
| *Remote sensors/CAPRICORN* | | | | |
| Cloud radar BASTA[a] Delanoë et al. (2016), UCAR/NCAR EOL (2018a) | W-band cloud radar 94.95 GHz. Mounted on a stabilized platform to endure vertical radar points | Temporal resolution 1min and four vertical resolutions (12.5, 25, 100, 200 m). Minimum valid signal distance 40 m, maximum observable altitude 12 km minimum detectable radar reflectivity –45 dBZ at 1 km | Reflectivity, Doppler velocity | Rain attenuation |
| *In situ/CAPRICORN* | | | | |
| ODM470 Disdrometer Klepp et al. (2018) | OceanRAIN[b] dataset. Emits a light from a diode at 880 nm and measure a volume of 120 mm in diameter. 1 minute resolution. 128 bins with logarithmic increase from 0.1 to 20 mm in diameter | Very light (0.01–0.09 mm/hr), light (0.1–0.99 mm/hr), moderate (1–9.99 mm/hr), intense (10–49.99 mm/hr), extreme (above 50 mm/hr) | Precipitation rate, intensity, and phase | Mixed and snow phase intensity |
| Radiosonde UCAR/NCAR EOL (2018b) | Radiosondes provided by CAPRICORN project | Resolution 1s. CAPRICORN I (II) had 1(4) sounding(s) on average per day | Temperature, relative humidity, zonal/meridional wind, surface pressure | Conditions are representative for the lower troposphere |
| *Remote sensors/SOCRATES* | | | | |
| Cloud radar HIAPER HCR[c] Vivekanandan et al. (2015), Romatschke and Vivekanandan (2022), UCAR/NCAR, EOL (2014), NCAR/EOL (2022) | W-band cloud radar 94.4 GHz | Resolution 30–150 m, sensitivity of −39.6 dBZ at 1 km, radial velocity uncertainty 0.2 m s$^{-1}$ at a vertical velocity of 2 m s$^{-1}$. Time: 0.5 s (corresponding to a spatial resolution of 83–105 m) | Reflectivity, Doppler velocity particle type | Drizzle <100 μm |
| *In situ/SOCRATES* | | | | |
| Two-Dimensional Cloud Probe (2DC) Wu and McFarquhar (2016), Wu and McFarquhar (2019) | Cloud optical array imaging probe with 64 photodiodes, a 25 μm resolution. Sample volume is a function of diameter (D) | D: >200 μm IWC: derived following Baker and Lawson (2006) | IWC, Nice, Dmm[d], cloud particle images | Limited data due to fogging. Probe's depth of field uncertain for small particle sizes |
| Cloud Droplet Probe (CDP) Lance et al. (2010), UCAR/NCAR EOL (2019) | Forward scattering probe that sizes particles using the Mie Theory. It emits a light from a laser beam and measures droplet size from amount of forward scattered light | Diameter: 2–50 μm | LWC, Nc | No ice detected. Uncertain sizing for non-spherical particles |
| Particle Habit Imaging and Polar Scattering Probe (PHIPS HALO) Abdelmonem et al. (2016), Schnaiter et al. (2018), Schnaiter (2018), Järvinen et al. (2022) | Two stereo microscopic cameras and detectors for measuring the scattering of light | Detecting particles from 20 to 700 μm of diameter (for ice, the lower diameter range is 50 μm) | Particle images, multi-angular scattering | Ice <100 μm and >700 μm. Droplets <20 μm and >700 μm |

**Table 1**
*Continued*

| Instrument name | Description | Measurement ranges | Key variables | Uncertainties |
|---|---|---|---|---|
| Rosemount Icing Detector (RICE) Baumgardner and Rodi (1989), UCAR/NCAR EOL (2019) | Piezoelectric sensor which detects presence of SLW from response of vibrating wire | Minimum SLW detected is 2 $\mathrm{mVm^{-1}}$ McFarquhar et al. (2013) | Voltage change | Above −4°C (due to dynamic heating of the probe) |
| Dropsonde UCAR/NCAR EOL (2018c) | Dropsondes funded by US National Science Foundation | Resolution 0.5 s. Eight dropsondes on average per flight | Temperature, relative humidity, zonal/meridional wind, surface pressure | Conditions are representative below 500 hPa |
| *State parameters/SOCRATES* | | | | |
| Vertical Cavity Surface Emitting Laser Hygrometer (VCSEL) Diao (2018), UCAR/NCAR EOL (2019) | Laser-based hygrometer | Water vapor concentrations | Relative humidity | Accuracy 6% Precision 1% |

[a]Bistatic Radar System for Atmospheric Studies (BASTA). [b]Ocean Rainfall And Ice-phase precipitation measurement Network (OceanRAIN). [c]High-Performance Instrumented Airborne Platform for Environmental Research (HIAPER). [d]Liquid Water Content (LWC), Ice Water Content (IWC), particle number concentration (Nc), Ice number concentration (Nice), and median mass diameter (Dmm). Super-Cooled Liquid Water (SLW) and particle size (D).

100 mm/hr (2018-01–27 22:00 to 23:13 UTC, and 2018-02-09 around 10:50 UTC). While these events have been classified as extreme, the actual precipitation rates are subject to very large uncertainties and are likely affected by the presence of ice and so should be treated with caution. To avoid an intensity overestimation by ice contaminated data, we exclude those two samples (which represent 0.021% of the total data) in the present analysis. The threshold is selected based on the inspection of the disdrometer time series.

A number of in-situ cloud microphysics data sets from the SOCRATES field campaign (Table 1) are also analyzed for a case study during one overflight transect above the RV Investigator (Section 3.4). Detailed information on the processing of in-situ cloud probe data and an overview of the uncertainties of the derived products and cloud parameters are provided in Y. Wang et al. (2020), McFarquhar et al. (2021), D'Alessandro et al. (2021), Baumgardner et al. (2017), and McFarquhar et al. (2017). It is worth highlighting that the 2DC is used in this analysis even though McFarquhar et al. (2021) stated that the use of the 2DS (which measures particles with similar sizes) was preferential because the 2DC suffered frequent fogging issues during SOCRATES. However, for the time period analyzed, the 2DS was suffering from technical issues. A careful inspection of the 2DC images for the analyzed period did not show any evidence of degraded image quality. For other time periods without degraded 2DC image quality and available 2DS data, Schima et al. (2022) showed that the 2DC had a slight underestimation of Nc by a factor varying between 0.5 and 0.75 (e.g., for flight on 4 February 2018). Corrections for out of focus particles, and shattered particles are made following techniques referenced above and incorporated into the University of Illinois/Oklahoma Optical Array Probe Processing Software (UIOOPS, McFarquhar et al. (2018)).

### 2.4. Synoptic and Thermodynamic Conditions

In this study, we characterize clouds and precipitation under various atmospheric conditions using three different, but complementary methods: clusters, cyclone composites, and cold front composites. The synoptic classification is based on the results found by Truong et al. (2020). They classified 2186 soundings deployed in four recent field campaigns using three methods (see below). We take the launch date and times (hereafter referred as sounding) and classification from 266 soundings from CAPRICORN 2016 and 2018. The cloud radar and disdrometer information is taken within ±1.5 hr of each sounding's launch time (e.g., if a sounding was launched at 2018-01-11 14:00 UTC, we then took the radar and disdrometer data between 2018-01–11 12:30 and 15:30 UTC). The length of the time window was chosen to ensure that the ship traveled less than 1°, yet provided enough samples for a robust statistical analysis. Time windows from ±0.5–4.0 hr were tested, but did not qualitatively change the results. Each sounding is classified as follows:

1. A k-means clustering technique using the thermodynamic information from the soundings. Truong et al. (2020) used 15 variables in this technique: temperature, relative humidity, zonal wind, meridional wind at three

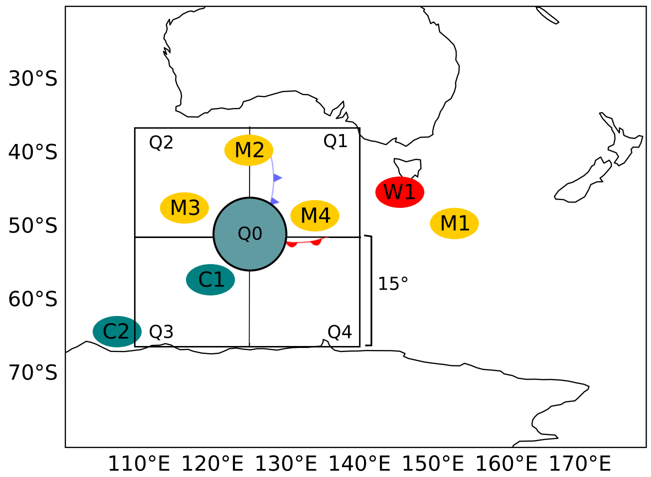

| Cluster | Characteristics |
|---|---|
| **W1** | Characterised by warm air advection from the Australian continent in pre-frontal regions north of ocean polar front |
| **M1** | Typically found in high-pressure systems (and ridging) in large scale subsidence |
| **M2** | Located at the north-northeast of the cyclone centre close to cold fronts but removed from the cyclone centre |
| **M3** | Represents the post-frontal area of a cold front, and northwest of the cyclone centre |
| **M4** | A warm front cluster |
| **C1** | Represents the conditions poleward of the ocean polar front near cyclones |
| **C2** | Indicates the conditions in the coastal Antarctica area, it can be located southwest of the cyclone centre |

**Figure 1.** A conceptual illustration of the seven thermodynamic clusters and their relationships to the extratropical cyclone, cold and warm front, derived in Truong et al. (2020). The red circle indicates the warm cluster (W1), Orange circles the medium clusters (M1–M4), and dark blue circles the cold clusters (C1–C2) and the proximity to Q0. Q0 represents the cyclone center, Q1–Q4 indicate the four cyclone quadrants. The red (blue) curve with half-circles (triangles) indicates the warm (cold) front. Note that cold and warm fronts are not always within the above illustrated quadrants. On the right, main cluster characteristics are also presented.

different levels (700, 850, and 925 hPa), and surface pressure, temperature, and relative humidity. This methodology is able to represent the midlatitude storm track region (W1, M1–M4), cyclones over the high-latitude SO (C1) and the sub-Antarctic (coastal) waters (C2) (Figure 1 for details on the main characteristics of each cluster).

2. Cyclone detection; we use the University of Melbourne (UM) cyclone detecting and tracking scheme. For the UM scheme we take the 3-hourly ERA5 reanalysis product at a 0.25° spatial resolution (Murray & Simmonds, 1991). The UM cyclone tracking and detecting method is a well-established global method for cyclone detection (Pepler et al., 2020). For a given cyclone, we define four quadrants as in Lang et al. (2018) (Q1–Q4; within a distance up to 15° from the cyclone center) and one center (Q0; representing all soundings within 5° distance of the cyclone center). Each sounding is classified to the nearest 3-hourly date resulting from this classification.
3. Frontal activity using the method of Berry et al. (2011) with hourly ERA5 reanalysis at a 0.75° spatial resolution. Only cold fronts within 15° from the RV Investigator are considered. The cold Frontal sections are defined as distances within 2.5° of the front line, whereas the pre-frontal (post-frontal) sections are between −15 and −2.5° (2.5 and 15°). We take the nearest hour to the sounding and perform the frontal classification.

A schematic diagram that describes the general relationships between the various classifications is presented in Figure 1. It is worth noting that the weather conditions over the SO are highly variable. Thus, the location of warm and cold fronts relative to the cyclone center can differ significantly from the classic diagram shown in Figure 1. Also, the spatial and temporal resolution of ERA5 used for the cyclone and front detection can induce uncertainties in their exact positions. Nevertheless, the seven clusters extend beyond the common storm-track weather patterns typically represented in the cyclone and front composites.

### 2.5. Methods

To provide insights into the thermodynamic and microphysical properties of the observed clouds and precipitation, Contoured Frequency by Altitude Diagrams (CFADs, Yuter and Houze (1995)) and their variants, Contour Frequency by Temperature Diagrams (CFTDs, Huang et al. (2015)) are constructed from the RV Investigator cloud radar reflectivity for the various synoptic classifications. These diagrams have been widely used (Bodas-Salcedo et al., 2011; Finlon et al., 2020; Huang et al., 2015; Mace & Protat, 2018a; McFarquhar et al., 2021; Zhou et al., 2020) since they do not assume prior statistics (Yuter & Houze, 1995). They can be used for non-Gaussian and multimodal distributions such as radar data because they preserve information in the frequency distribution (Yuter & Houze, 1995). Additionally, we consider the median radar reflectivity as a function of the Doppler velocity and temperature (altitude). We note that the CFTD is able to define the melting level (by the 0°C isotherm), which may be of particular interest. Rainfall speeds are typically between −10 and −5 $ms^{-1}$ (Foote & Du Toit, 1969). For snow they are between −2 and 0.5 $ms^{-1}$ (Mitchell, 1996). A sharp Doppler transition in the median contour plots can be interpreted as the melting layer height if we assume that vertical air motions are smaller than fall speeds. The BASTA cloud radar data set includes an interpolated temperature variable from ERA-Interim that is used for the CFTD. The cloud mask product from the CAPRICORN cloud radar and lidar information (Huang et al., 2019) is used to estimate cloud occurrence frequency, CF [%], which is defined as the ratio between the time when cloud was observed over the ship and the total length of the time-window for a given synoptic condition.

The radar reflectivity is a measure of the sixth moment of the drop size distribution. Thus, the received power by the cloud radar is affected by the particle size observed such that the radar is sensitive to large particles because non-Rayleigh scatter effects become important for precipitation sized particles. As such the composite structures of the radar reflectivity and Doppler velocity can be examined jointly to infer plausible dominant ice growth processes, when the known limitations of a single-frequency cloud radar are properly taken into account. For instance, given the low density and large size of ice aggregates compared to liquid drops, aggregation is likely dominant when the reflectivity in the temperature range (−30 to −15°C) increases more uniformly toward lower altitudes (higher temperatures) (Bodas-Salcedo et al., 2011; Franklin et al., 2013), while the Doppler velocity remains relatively small (becoming more negative; between −1 and 0 $ms^{-1}$, Thompson et al. (2008)). On the other hand, strong riming may be occurring when moderate-to-strong reflectivities are accompanied by higher fall velocities, particularly at the sub-freezing temperature range in a convective environment where supersaturation with respect to liquid water is more easily achieved (Alexander et al., 2021; D'Alessandro et al., 2021). Thus, our interpretation will be based on where we see these patterns and the reflectivity and Doppler velocity thresholds described in Section 2.2.

We consider both surface and in-cloud precipitation. The ship-borne disdrometer records are used to determine the 1-min surface precipitation rates and the thermodynamic phase (see Section 2.3). In-cloud precipitation is defined as precipitation that is developed in clouds but does not reach the surface at the ship. In-cloud precipitation is considered when the minimum radar reflectivity profile above 0.2 km exceeds −15 dBZ (lower threshold for drizzle), and the disdrometer detects dry conditions at the surface. This characterization is only qualitative given the limitation on estimating precipitation rates with the cloud radar. We note that in-cloud precipitation has the potential to advect far downwind in the strong westerly winds of the SO storm track. Thus in-cloud precipitation does not necessarily indicate sub-cloud evaporation.

## 3. Cloud and Precipitation Properties

### 3.1. Cloud Radar Statistics Under the Seven K-Means Clusters

The CFTD/CFAD of the W1 cluster (warm air advection in the pre-frontal regions north of ocean polar front) is characterized by a broad distribution of clouds across the temperature range from −30 to 15°C, reaching altitudes up to almost 8 km (Figures 2a and 2c). The large fraction of warm clouds (greater than 0°C) features a wide reflectivity spectrum between −25 and 10 dBZ, indicating a large variability ranging from non-precipitating to drizzling, to precipitating clouds (Wood et al., 2009). Precipitating warm clouds typically have Doppler velocity less than −3 $ms^{-1}$ with median reflectivities higher than 5 dBZ, indicating heavy rain rates. Drizzling and non-precipitating warm clouds correspond to a weaker Doppler velocity; between 0 and −1 $ms^{-1}$ (Figures 2b and 2d).

The W1 average melting layer height is identified at around 3.5 km, which is the highest of all clusters (Figure 2 right column for comparison). Between −10 and 0°C, precipitation-size particles dominate the reflectivities, with values between −10 and 5 dBZ (likely mixed-phase clouds (Bodas-Salcedo et al., 2011, 2014; Naud et al., 2014)), whereas clouds at temperatures less than −10°C have a core of strong reflectivities from −10 to 0 dBZ. Likely evidence of large ice particles (above 5 dBZ) associated with convective updrafts can be identified with Doppler velocities around 1 $ms^{-1}$ at −20°C (Figure 2b). Far less frequent, non-precipitating clouds (likely cirrus) are also present, as shown in the second branch with temperatures below −10°C (above 6 km) and reflectivities lower than −15 dBZ. Surface precipitation is recorded approx. 6% of the time, predominantly very light/light precipitation (below 0.99 mm/hr) and liquid phase (Table 2). Overall, these cloud and precipitation characteristics are consistent with warm air advection featuring a warm and moist troposphere.

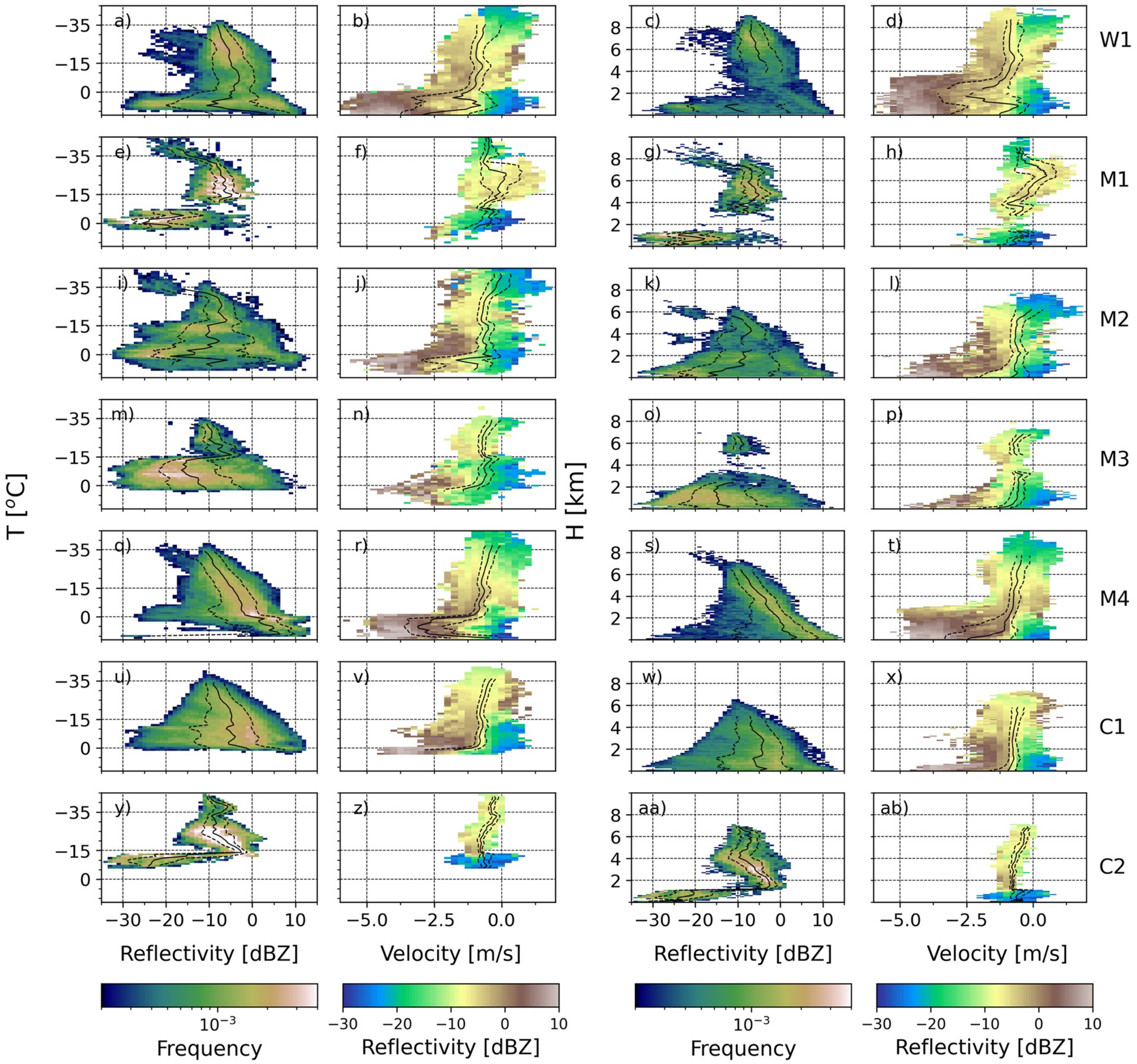

**Figure 2.** From left to right Bistatic Radar System for Atmospheric Studies cloud radar reflectivity Contour Frequency by Temperature Diagram and reflectivity median value as a function of temperature and Doppler velocity, followed by the same figures for altitude. Dotted lines are the 25% and 75% percentile, line the 50% percentile of the abscissa variable. From top to bottom, clusters W1 (warm air advection), M1 (high pressure), M2 (cold front), M3 (post-front), M4 (warm front), C1 (high-latitude cyclone center), and C2 (coastal Antarctica). All during the Clouds Aerosols Precipitation Radiation and atmospheric Composition Over the Southern Ocean I and II, synoptic conditions are classified by a k-means clustering method.

The high-pressure cluster M1 (Figures 2e–2h) features the lowest cloud occurrence (CF 62%, see Table 2). A discontinuous dipole-like structure is evident in the CFTD/CFADs, representing two dominant disconnected cloud types: non-/lightly precipitating boundary layer clouds (likely closed mesoscale cellular convection as reported in Lang et al. (2020), Lang et al. (2022)) with Doppler velocities between 0 and $-2$ ms$^{-1}$; and mid-level clouds with in-cloud precipitation that does not reach the lower troposphere. The latter features a high concentration around −20°C and −5 dBZ, which suggests small precipitation-size particles, possibly mixed phase. Cirrus clouds are also present (below −30°C and with reflectivities below −10 dBZ). Precipitation measurements suggest virtually dry conditions at the surface, and in-cloud precipitation about 7% of the time (Table 2). The disdrometer measurements and the CFAD/CFTD cloud patterns are generally consistent with the M1 conditions inferred from the average sounding profile (Figure 3 in Truong et al. (2020)).

**Table 2**

*Minute Resolution OceanRAIN Disdrometer Surface Precipitating Time ($P_s$ [%]), Precipitating Median ± Interquartile Range Intensity ($\tilde{I} \pm IQR$ [mm/hr]), and Percentages of Surface Very Light ($P_{vl}$), Light ($P_l$), Moderate ($P_m$), Intense ($P_i$), and Extreme ($P_e$), as Well as the Percentage of Liquid, Snow, and Mixed-Phase Precipitation*

| | | **Disdrometer** | | | | | | | | | | **Radar-lidar** | |
|---|---|---|---|---|---|---|---|---|---|---|---|---|---|
| Synoptic | S | $P_s$ [%] | $\tilde{I} \pm IQR$ [mm/hr] | $P_{vl}$ [%] | $P_l$ [%] | $P_m$ [%] | $P_i$ [%] | $P_e$ [%] | Liquid [%] | Snow [%] | Mixed [%] | $P_c$ [%] | CF [%] |
| W1 | 39 | 6.30 | 0.27 ± 0.9 | 31.06 | 44.71 | 23.29 | 0.94 | 0.00 | 100.00 | 0.00 | 0.00 | 13.08 | 83.80 |
| M1 | 26 | 1.33 | 0.05 ± 0.04 | 95.08 | 4.92 | 0.00 | 0.00 | 0.00 | 100.00 | 0.00 | 0.00 | 6.53 | 61.89 |
| M2 | 41 | 4.54 | 0.24 ± 0.55 | 28.35 | 55.49 | 15.85 | 0.30 | 0.00 | 89.02 | 0.61 | 10.37 | 6.69 | 71.86 |
| M3 | 37 | 4.75 | 0.1 ± 0.34 | 49.21 | 36.19 | 11.75 | 2.86 | 0.00 | 92.06 | 1.27 | 6.67 | 9.50 | 88.38 |
| M4 | 21 | 44.92 | 0.37 ± 0.78 | 28.10 | 51.36 | 20.48 | 0.00 | 0.06 | 96.81 | 1.77 | 1.42 | 10.60 | 92.19 |
| C1 | 91 | 20.05 | 0.15 ± 0.52 | 40.17 | 44.22 | 13.19 | 1.50 | 0.91 | 47.13 | 40.39 | 12.47 | 7.19 | 86.95 |
| C2 | 11 | 0.00 | 0.00 ± 0.00 | 0.00 | 0.00 | 0.00 | 0.00 | 0.00 | 0.00 | 0.00 | 0.00 | 21.57 | 85.41 |
| Q0 | 57 | 23.15 | 0.21 ± 0.52 | 32.38 | 53.12 | 14.24 | 0.22 | 0.04 | 67.98 | 21.76 | 10.26 | 8.50 | 92.22 |
| Q1 | 40 | 14.79 | 0.28 ± 0.77 | 35.17 | 45.54 | 19.09 | 0.10 | 0.10 | 90.21 | 4.84 | 4.94 | 10.25 | 70.70 |
| Q2 | 39 | 10.57 | 0.17 ± 0.88 | 40.91 | 35.81 | 20.66 | 2.62 | 0.00 | 94.49 | 2.75 | 2.75 | 7.78 | 84.45 |
| Q3 | 36 | 6.72 | 0.09 ± 0.1 | 55.89 | 39.26 | 4.62 | 0.23 | 0.00 | 25.87 | 73.67 | 0.46 | 8.14 | 76.91 |
| Q4 | 29 | 18.26 | 0.55 ± 1.04 | 15.55 | 53.89 | 23.84 | 3.78 | 2.94 | 78.00 | 5.57 | 17.44 | 12.03 | 87.50 |
| Pre | 45 | 10.27 | 0.19 ± 0.42 | 30.59 | 63.46 | 5.94 | 0.00 | 0.00 | 71.30 | 28.70 | 0.00 | 8.37 | 82.30 |
| Post | 87 | 15.69 | 0.20 ± 0.66 | 34.47 | 46.62 | 17.95 | 0.88 | 0.08 | 72.55 | 16.60 | 10.84 | 7.57 | 78.02 |
| Frontal | 26 | 23.13 | 0.40 ± 0.93 | 32.44 | 43.19 | 23.35 | 1.02 | 0.00 | 73.21 | 17.05 | 9.73 | 3.93 | 95.38 |

*Note*. Precipitating time inside clouds, and not reaching the surface ($P_c$[%]) estimated from the 1 min mean W-band cloud radar. Cloud Occurrence Frequency (CF) defined using the cloud mask from the cloud radar/lidar data set on a 1-min resolution. All during CAPRICORN I and II classified by different synoptic scenarios: k-means clustering, distance to cyclone and front. Note that the number of soundings (S) used for the identification of each scenario is highlighted.

Moving to the cold front (M2) cluster, the radar reflectivity CFTD/CFAD has a broad distribution (−25 to 15 dBZ), spanning from temperatures above 10°C down to about −15°C, hinting at a wide range of hydrometeor types/sizes, cloud types, microphysical processes, and convective/stratiform precipitation (Figures 2i and 2k). Strong radar reflectivities (greater than 5 dBZ) associated with Doppler velocity around/above 1 ms$^{-1}$ are present between −20 and −5°C, consistent with strong ice production within the convective updraft (see dark brown colors near greens in Figure 2j). There are also some fast-falling particles, faster than −3 m/s, with reflectivities around 5 dBZ (Figures 2j and 2l). Between −30°C and −15°C, the slope of the mean reflectivity suggests ice growth. At around −35°C (6 km), the low reflectivities and narrow frequency distribution seem consistent with the dominance of small ice particles, probably formed by heterogenous nucleation ((Zhao et al., 2021; Figures 2i and 2k). Although one might expect considerable precipitation for the cold front cluster, the disdrometer indicates surface precipitation only 5% of the time: predominantly light (55%) and liquid (89%), followed by mixed phase (18%). The in-cloud precipitation is also only present ~7% of the time. While somewhat counter-intuitive, the analysis suggests that the M2 cluster might be dominated by pre-frontal multi-level clouds that do not actively produce intense precipitation.

The radar reflectivity CFTD/CFAD for the cold post-frontal (M3) cluster has a broad distribution in the lower troposphere, which narrows significantly toward higher (lower) altitudes (temperatures), signaling the dominance of a relatively shallow cloud population at temperatures greater than −15°C and a detached cloud between −35 and −15°C (Figures 2m and 2o). While non-precipitating clouds prevail in the shallow cloud regime, there are strong radar reflectivities (greater than 5 dBZ) associated with strong negative Doppler velocities (smaller than −2 ms$^{-1}$) between −10 and 0°C, consistent with the formation of large particles (Figures 2n and 2p). Such characteristics are congruent with in-situ observations in the Hallett-Mossop temperature zone (rime splintering between −8 and −3°C) shown in several previous studies for a similar synoptic environment (Huang et al., 2017, 2021), commonly associated with the open mesoscale cellular convection (Lang et al., 2021, 2022). Surface precipitation of this cluster is recorded 5% of the time, featuring dominantly very light/light precipitation and dominantly liquid phase. The bulk of the clouds residing below 2.5 km is consistent with a strong temperature inversion at approx. 780 hPa for the M3 cluster (Figure 3 in Truong et al. (2020)).

The M4 cluster (warm front) produces the largest CF (92%). The radar reflectivity CFTD/CFAD showcases the typical arc shape of large-scale deep convection (Dodson et al., 2018), where the mean reflectivity increases monotonically toward higher temperatures and lower altitudes, which also indicates high water content and likely the presence of aggregation (Bodas-Salcedo et al., 2011; Figures 2q and 2s). There is a visible enhancement of reflectivity below the melting level in the CFTD, but not evident in the CFAD. This pattern suggests that the melting level in the M4 soundings varies across a range of altitudes. The frequency distribution in M4 is narrower than that in the M2 (cold front) cluster, indicating more uniform microphysical processes (likely dominated by aggregation, mainly between −15 and 0°C) as well as hydrometeor types. Strong reflectivity values in the warm rain region indicate precipitation with negative velocities between −3 and −5 ms$^{-1}$ (Figures 2q–2t). This cluster registers the highest precipitation percentage (approx. 45% at the surface and 11% in clouds). The disdrometer records predominantly liquid phase (occasionally below 0°C). Overall the disdrometer and CFAD/CFTD information is consistent with a typical warm front scenario as discussed in Truong et al. (2020). The M4 and W1 clusters share some similarities in the CFAD/CFTD patterns, based on the nature of these two clusters we hypothesize that the W1 clouds evolve into M4 clouds as it moves further south. Additional analyses would be needed to confirm this process.

The radar reflectivity CFTD/CFAD for the C1 cluster (high-latitude cyclone over the SO) features an absence of warm clouds but a broad spectrum below freezing temperature, which indicates a wide variety of hydrometeors (Figures 2u–2x). Unlike previous clusters, there is no clear division between the cloud layers. Similar to M3, some of the high reflectivities coincide with fast falling velocities (smaller than −2 ms$^{-1}$) within the Hallett-Mossop temperature zone, possibly indicating the presence of rimed particles and/or graupel, although further observations are needed to confirm their presence. High reflectivities associated with a Doppler velocity of around 1 ms$^{-1}$ were also detected close to −15°C, suggestive of active convection. This is consistent with the expected behavior of C1, which resides typically close to a cyclone center. Precipitation data show that C1 has the highest mean intensity from all clusters, although the absolute values are subject to higher uncertainties given the highest fraction of snow detected at the surface (about 40%).

Contrasting to the C1 cluster, the coastal Antarctica C2 cluster CFTD/CFAD indicates two distinct cold cloud types (Figures 2y and 2aa). One is the non-precipitating shallow clouds (below 1 km or greater than −15°C) with radar reflectivities below −15 dBZ and Doppler velocities between −2 and 0.5 ms$^{-1}$ (Figures 2z and 2ab). The other represents the mid-level cloud type which is more prevalent. The magnitude and slope of the reflectivity frequencies between −30 and −15°C once again imply ice growth. The C2 cluster has no precipitation at the surface, consistent with the low humidity in the lower troposphere reported in Truong et al. (2020). However, in-cloud precipitation is present almost 22% of the time in the mid-level clouds (Table 2), which suggests strong evaporation and/or sublimation in the lower troposphere, likely associated with the descending, dry, katabatic winds off the Antarctic coast. Note that the number of soundings for this cluster is relatively small (11) compared to the others.

It should be noted that the cluster classification performed by Truong et al. (2020) focused on the lower free troposphere, only employing soundings information up to the 700 hPa level. In general, the upper troposphere has stronger winds and is not necessarily directly linked to the lower troposphere. We note the common presences of clouds from 5 to 8 km along the storm track (M1–M4). The strong winds in the upper-troposphere can readily advect clouds across the clusters. We also note that the cloud radar might underdetect the thin, non-precipitating liquid clouds, particularly in the lower troposphere, but this limitation is not expected to affect our key findings.

### 3.2. Cloud Radar Statistics Under Cyclone Quadrants Conditions

Moving to the analysis with respect to cyclone quadrants, overall the CFAD/CFTD patterns corresponding to each quadrant are less distinct than those segregated by clusters (Section 3.1). Nevertheless, the zero quadrant (Q0) reflectivity CFTD/CFAD characteristics largely resemble the C1 counterparts, except that a small fraction of warm clouds are also present (Figures 3a and 3c). This may be explained by the fact that Q0 includes all cyclone centers detected during the field campaigns, not only those limited to the high-latitude SO where clouds

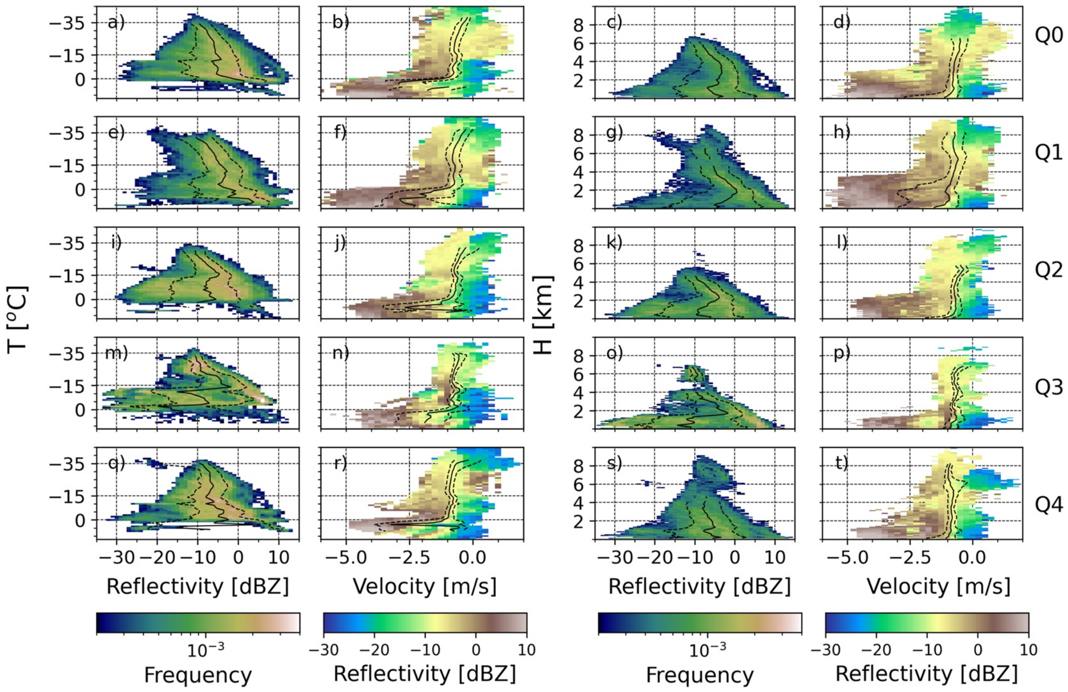

**Figure 3.** Same as Figure 2 but segregated by cyclone sectors.

are generally much colder. Q0 also includes a portion of M2 (18%) and M4 (11%) clusters where warm clouds are not uncommon. The disdrometer information is consistent with the CFTD/CFAD analysis for Q0 in terms of precipitation characteristics.

Q1 resembles the M4 and M2 clusters, with differences noted due to the large variability of the cold/warm front location with respect to the cyclone center. Thus, the Q1 quadrant represents only a subset of the total number of cold and warm frontal conditions, whereas the M2 and M4 clusters showcase a more unambiguous representation. The Q1 CFTD/CFAD radar reflectivity has an arc shape between 5 and −10 dBZ (typical of deep convection, Dodson et al., 2018; Figures 3e–3h). Warm clouds are mainly precipitating clouds with strong Doppler velocities between −6 and −2 ms$^{-1}$. Between −5 and 0°C there is a band ranging from 0 to −15 dBZ, probably representing mixed-phase conditions.

Q2 is likely dominated by shallow clouds at temperatures greater than −15°C (3 km). The CFAD/CFTD distributions for Q2 are similar to those of the M3 cluster, which is expected since the M3 cluster represents the post-frontal conditions. Several high-frequency cores are present between −15 and 0°C, indicating the presence of a variety of microphysical mechanisms (Figures 3i–3l). Strong radar reflectivities (around 5 dBZ) are seen with Doppler velocities greater than −2 ms$^{-1}$, indicating the presence of dense particles (e.g., possibly graupel or rimed particles, as also noted for M3), as well as a mixture of liquid and ice precipitation. The surface precipitation characteristics also resemble those of M3.

Q3 and Q4 conditions are less explored in the literature. Our analysis suggests that Q3 is a hybrid of C1 and M3 conditions (Figures 3m and 3o) while Q4 most commonly represents C1 and, to a lesser extent, W1 (Figures 3q–3t). Interestingly, however, Q3 has the lowest precipitation intensity among all cyclone sectors, while Q4 features the highest intensity. Q3 surface precipitation is dominated by snow, while liquid phase precipitation is most commonly observed for Q4 (mostly SLW). This may not be a surprise given the colder nature of Q3 associated with a stronger southerly winds.

It is worth noting that the 15° box per quadrant may not be the best threshold for discriminating the cyclone conditions, as the nearest cyclone may not necessarily be the dominant feature at a given sounding. Nevertheless, we tested three different sizes (from 10 to 20° per quadrant) and the 15° was the distance that allowed a good number of sounding per quadrant. Our results are not qualitatively impacted by this threshold.

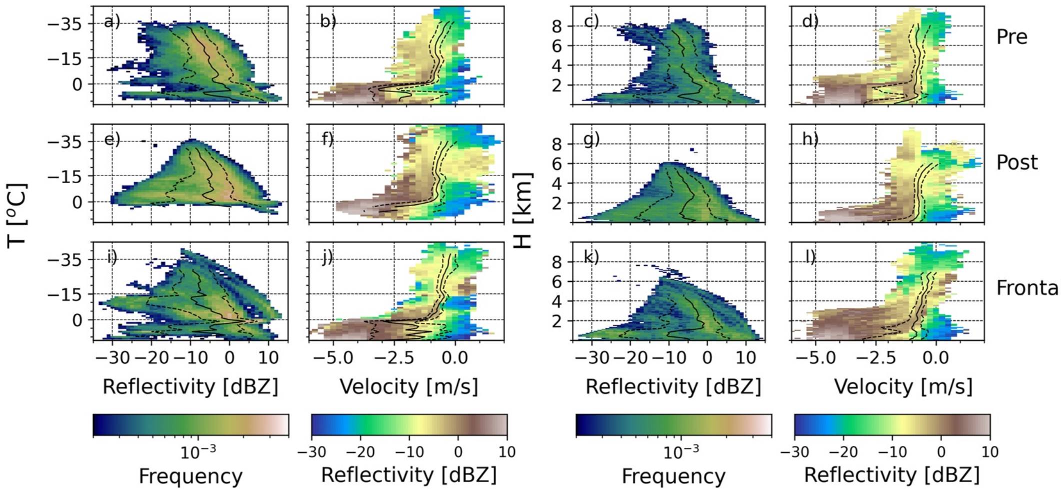

**Figure 4.** Same as Figure 2 but segregated by distance to cold front.

### 3.3. Cloud Radar Statistics Under Cold Front Distance Conditions

The analysis associated with cold front composites has significantly fewer soundings compared to the k-means clustering analysis (108 less, see Table 2). The pre-, post-, and frontal classifications all have a hybrid of different clusters, suggesting that this methodology has limited skills in segregating cloud regimes.

The radar reflectivity CFTD/CFAD in the pre-frontal condition resemble that of the W1 cluster (Figure 4). It should be noted, however, that the W1 cluster only represents the pre-frontal air mass with strong warm advection north of the ocean polar front, while the pre-frontal conditions could happen across latitudes. The post-frontal CFTD/CFAD distributions contain mainly some of the C1, M2, and M3. Finally, the cold frontal condition is composed primarily of almost the same proportion of C1 and W1 clusters.

Turning to precipitation, the pre-frontal condition has a higher fraction of warm rain, evidenced by the high reflectivity values at Doppler velocities stronger than $-3$ ms$^{-1}$. This classification also has the highest fraction of snow, according to the surface measurements. The frontal conditions have the highest precipitation intensity among the three, which is to be expected given the dominance of C1 (31%) and W1 (27%) clusters.

To summarize, the K-means clustering methodology is shown to be highly skillful in sorting/defining cloud and precipitation regimes. The cyclone and frontal composite methods produced more ambiguous results, despite their extensive applications in the literature. In general, clouds in the upper free troposphere are less distinct across all classifications, which is not unexpected given the common decoupling of the upper troposphere dynamics from the surface meteorology that is used to drive the thermodynamics and synoptic classifications.

## 4. Case Study: GV Aircraft Microphysical Characteristics

In this section, we analyze a segment of the third flight (RF03) of the SOCRATES mission to evaluate, as a case study, our interpretation of remote-sensing observations from the CAPRICORN campaign. We selected the period when the GV aircraft was closest to the RV Investigator (between 2018 and 01-23 00:50 and 01:18 UTC), which is defined by the time the GV aircraft did one ascending (descending) leg toward (away from) the RV Investigator, sampling the same synoptic conditions (Figure 5). Since the shipborne cloud radar has a lower temporal resolution than the airborne one, we selected an extended period for the comparison while ensuring that the ship was under the same synoptic conditions (between 2018 and 01–22 23:40 and 2018-01-23 02:50 UTC).

Flight RF03 included one constant leg in the vicinity of the ship lasting for about 7 min at 6 km, launching a dropsonde west of the RV Investigator at 2018-01-23 01:02 UTC. The flight dropsonde is classified as a M4 cluster (Figure 6). Equally, the radiosonde from the RV Investigator, which was launched about 10 min before the approach of the aircraft (2018-01-23 00:52 UTC), is also classified as M4. This is also consistent with the frontal and cyclone detection and the Himawari-8 satellite cloud type classification, with Altostratus, Nimbostratus and

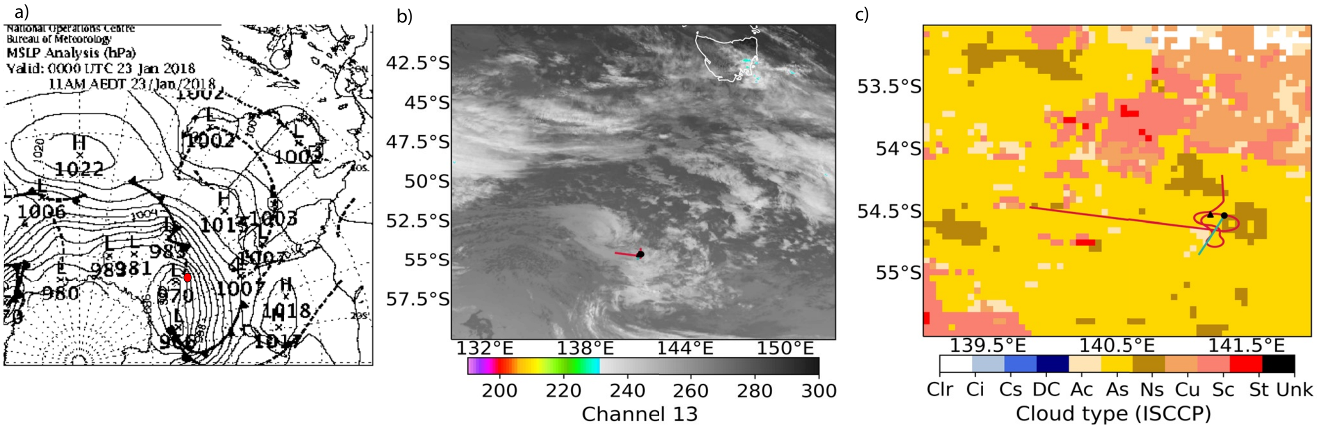

**Figure 5.** (a) Mean Sea level Pressure (MSLP) analysis of the Australian Bureau of Meteorology (BoM) for 2018-01-23 00 UTC. Red dot indicates the approximate location of the Research Vessel (RV) investigator and the Gulfstream V (GV) aircraft. (b) Himawari-8 brightness temperature in Kelvin (channel 13), and (c) cloud type classification from the Japan Aerospace Exploration Agency for 2018-01-23 00:50 UTC; black triangle (square) shows the location of the dropsonde (radiosonde). The red line indicates the GV aircraft track during the period (2018-01-23 00:50 to 01:18 UTC). Blue line represents the RV Investigator location while measuring the same type(s) of clouds (2018-01-22 23:40 and 2018-01-23 02:50 UTC).

occasionally multi-layer cloud systems dominating the sampling area (Figure 5). The Mean Sea Level Pressure (MSLP) analysis chart from the BoM indicates the ship and the aircraft were located near a warm front at 2018-01-23 00:00 UTC, although at this time a low pressure center to the south was in close proximity. Note that the MSLP snapshot is earlier than the sampling period and the warm front would have been closer to the RV Investigator by the sampling time.

When using the other two synoptic classifications (cyclone and frontal composites), the sampled areas were in Q0 (at an approximate distance of 4° north 0.04° west of the cyclone center) and pre-frontal (at a distance of about 4° ahead of the cold front) conditions. When the ship and the aircraft were close, the radiosonde, the dropsonde, the radar and lidar observations show characteristics comparable to the M4 cluster description. Both sondes indicate strong north-westerly winds and saturated conditions below 500 hPa, indicating the presence of precipitating clouds (Figure 6). The disdrometer aboard the RV Investigator recorded primarily liquid precipitation with an

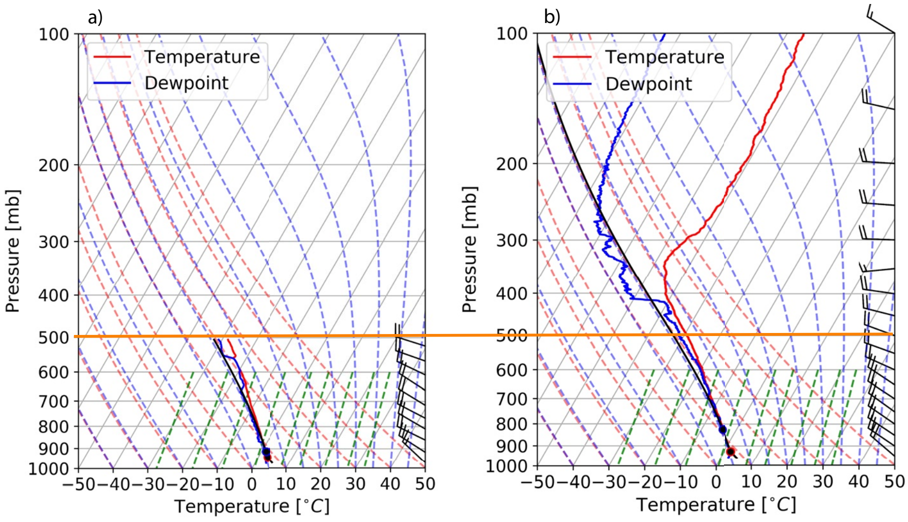

2018-01-23 01:02:48 to 2018-01-23 01:32:02

2018-01-23 00:52:03 to 2018-01-23 01:54:57

**Figure 6.** (a) Dropsonde sounding profile from the Gulfstream V (GV) aircraft launched at 2018-01-23 01:02 UTC. (b) Radiosonde sounding released from the Research Vessel (RV) Investigator at 2018-01-23 00:52 UTC. Orange line indicates the altitude of the GV aircraft.

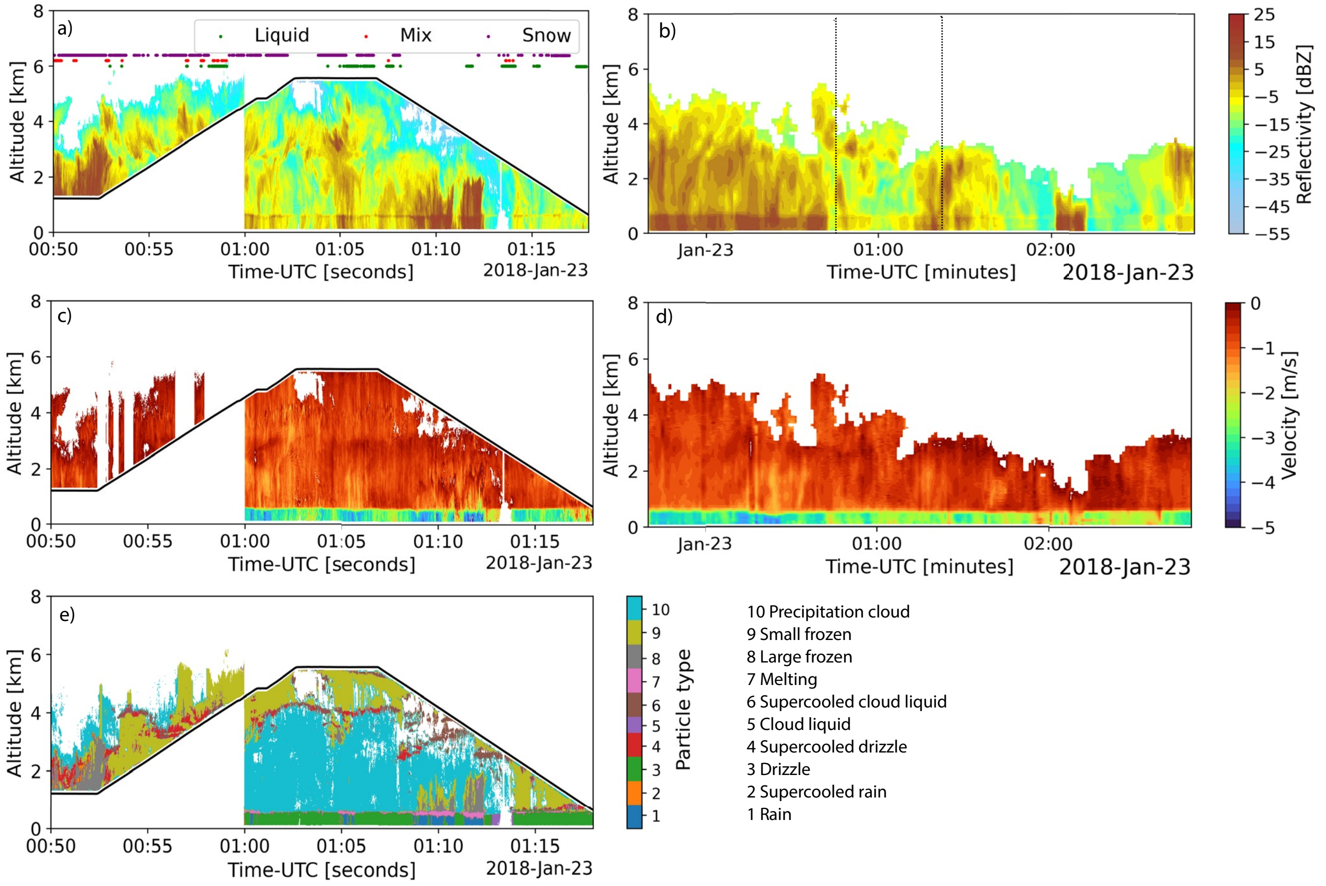

**Figure 7.** Left (right) panel shows the High-Performance Instrumented Airborne Platform for Environmental Research (HIAPER) (Bistatic Radar System for Atmospheric Studies (BASTA)) data from (a–b) the cloud radar reflectivity (dBZ) (Contours), black line indicates the Gulfstream V (GV) altitude and colored lines/dots the phase classification according to Schima et al. (2022). Dashed lines in (b) enclose the HIAPER time period. (c–d) Doppler velocity; and (e) Particle type. Between 2018 and 01–23 00:50 and 01:18 UTC for HIAPER (between 2018 and 01–22 23:40 and 2018-01-23 02:50 UTC for BASTA). Note that the Research Vessel (RV) Investigator needs more time to sample a similar area as the GV aircraft.

intensity between very light to light and a median precipitation intensity of 0.14 ± 0.31 mm/hr. This is weaker than the median intensity in the M4 cluster, but still within the natural variability (0.21 ± 0.52 mm/hr, Table 2).

The HIAPER radar observations show that the sampled clouds were commonly precipitating, with a melting layer located at around 600m above sea level (Figure 7). The Doppler velocity, ranging from 0.28 and −1.38 $\mathrm{ms}^{-1}$, is predominantly negative and decreases further when reaching the melting layer (down to values near −5 $\mathrm{ms}^{-1}$; Figure 7c). According to the HIAPER HCR/HSRL cloud phase product, there is a large variability of particle types in the descending leg and small ice particles with SLW drizzle in the ascending leg (Figure 7e).

The radar reflectivity CFAD/CFTD features a broad distribution, suggesting a large variety of hydrometeors and microphysical types/processes (Figure 8). Three modes of high frequency are visible: the first mode lies between −30 and −15°C (2.5–5 km), characterized by reflectivity increasing from −25 to 0 dBZ toward higher temperatures, likely suggesting particle growth primarily via aggregation. The second mode is located at −15 and −5°C (0.7–2 km), with reflectivities around −12 and 0 dBZ, also suggesting ice growth. The third mode is a small core near the melting layer, likely indicating the coexistence of SLW and small ice particles. In the warm clouds, the radar reflectivities peak in the range of −15 to 0 dBZ, indicating lightly precipitating clouds. Although less frequent, the cloud radar also detects strong precipitation in the warm cloud region, where reflectivities above 5 dBZ, with Doppler velocities stronger than −3 $\mathrm{ms}^{-1}$, are present near the melting layer (Figures 8a and 8c). The shipborne CFAD/CFTD patterns share some similarities with the GV counterparts, although the modes are less distinct in the former probably due to the lower time resolution of the observations. Both the airborne and shipborne CFAD/CFTD patterns provide evidence of deep cloud layer(s) and particle growth toward lower altitudes

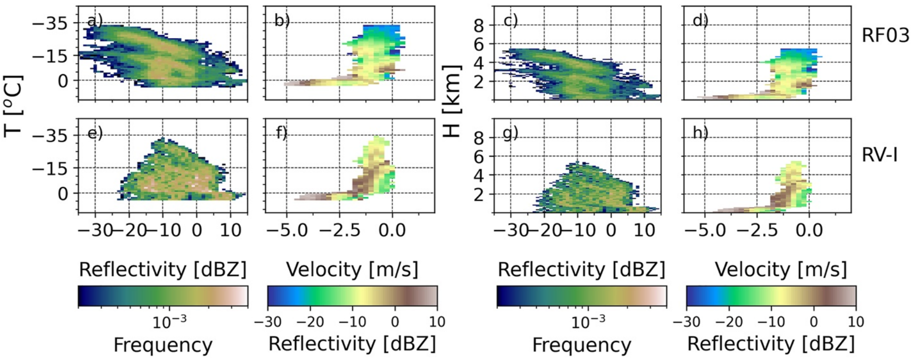

**Figure 8.** Same as Figure 2 but for the High-Performance Instrumented Airborne Platform for Environmental Research cloud radar during the third flight of the Southern Ocean Cloud Radiation and Aerosol Transport Experimental Study field campaign (RF03) and the Bistatic Radar System for Atmospheric Studies cloud radar during the Clouds Aerosols Precipitation Radiation and atmospheric Composition Over the Southern Ocean field campaign (RV-I). Note the time periods are different (2018-01-23 00:50 to 01:18 UTC vs. 2018-01-22 23:40 and 2018-01-23 02:50 UTC; but both are under the same synoptic conditions (and cloud type).

via multiple mechanisms, broadly consistent with the M4 cluster and pre-frontal composite results as discussed in Section 3.

The in-situ aircraft observations provide (Figure 9) direct evidence of the microphysical properties that can help evaluate our interpretation from Figure 8. Here, we examine one ascending and one descending leg in the proximity of the RV Investigator. The ascending leg penetrated through a deep cloud near a warm front, whereas the descending leg seemed to be coming through multi-layer clouds at the cloud edge and was not sampling much in cloud (Figure 7).

The in-situ phase classification based on Schima et al. (2022) indicates that ice phase was dominant along the ascent profile, about 76% of the in-cloud time, largely coinciding with the enhanced radar reflectivities, and hydrometeor classification by the HIAPER cloud phase product recorded in the vicinity of the flight path. The descent profile, on the other hand, features an intermittent presence of liquid or ice phase, consistent with the weaker reflectivities and the more tenuous structure of the cloud layers. The two vertical profiles show that the 2DC median mass diameter (Dmm) varies in the range between 150 and 3200 μm, suggesting the common presence of large particles, particularly along the ascent profile (Figure 9). Consistently, the 2DC instrument detected ice number concentrations (Nice) throughout the ascent profile (especially around 1.5 km, 3–3.7 km, and near 5.3 km) in the range of $7.5 * 10^{-5}$ to $1.9 * 10^{-3}$ $\mathrm{cm}^{-3}$, whereas little Nice was recorded during the descending leg (Figures 9c and 9i, note that the Nice is shown for ice phase clouds only due to the large uncertainties in the estimated Nice for mixed phase using the 2DC). It should be noted that the Schima et al. (2022) phase classification indicates more frequent ice phase in the descent profile than Figure 9h, because the classification used a combination of several cloud probes, not only the 2DC where only particles with sizes greater than 200 μm are considered. Liquid water content (LWC) profiles measured by the CDP probe are shown for liquid and mixed phase clouds (Figures 9d and 9i), providing more evidence on the phase characteristics. The descending leg further showcased typical boundary layer clouds (below 1 km; given the lower reached altitude).

The PHIPS particle habit images (Figure 10) indicate the frequent presence of rosettes at about 6 km or between −30 and −25°C. Some of the rosettes were bullet rosettes, while others have more complex structures. Between −20 and −10°C, the ice crystals were columns with some plate-like structures, rimed crystals, and ice of irregular habits (Figure 10). Between −5 and 0°C rimed particles and needles become more dominant, while water and rain droplets were typical at temperatures above 0°C. Snapshots of the particle images recorded by the Fast 2DC particle probe at different altitudes/temperatures also indicate a large variety of particle habits, broadly consistent with those recorded by the PHIPS instrument. Overall, the observed ice habits are consistent with what has been reported in the literature for deep clouds over mid and high latitude oceans (Bailey & Hallet, 2009; Kikuchi et al., 2013). Inspection of the 2DC images did not show evidence for pervasive amounts of supercooled drizzle (SLD). However, there is a possibility that small amounts of SLD were present (see Figure 7e) due to ambiguity in interpreting the shapes of the 2DC images, and hence in the phase.

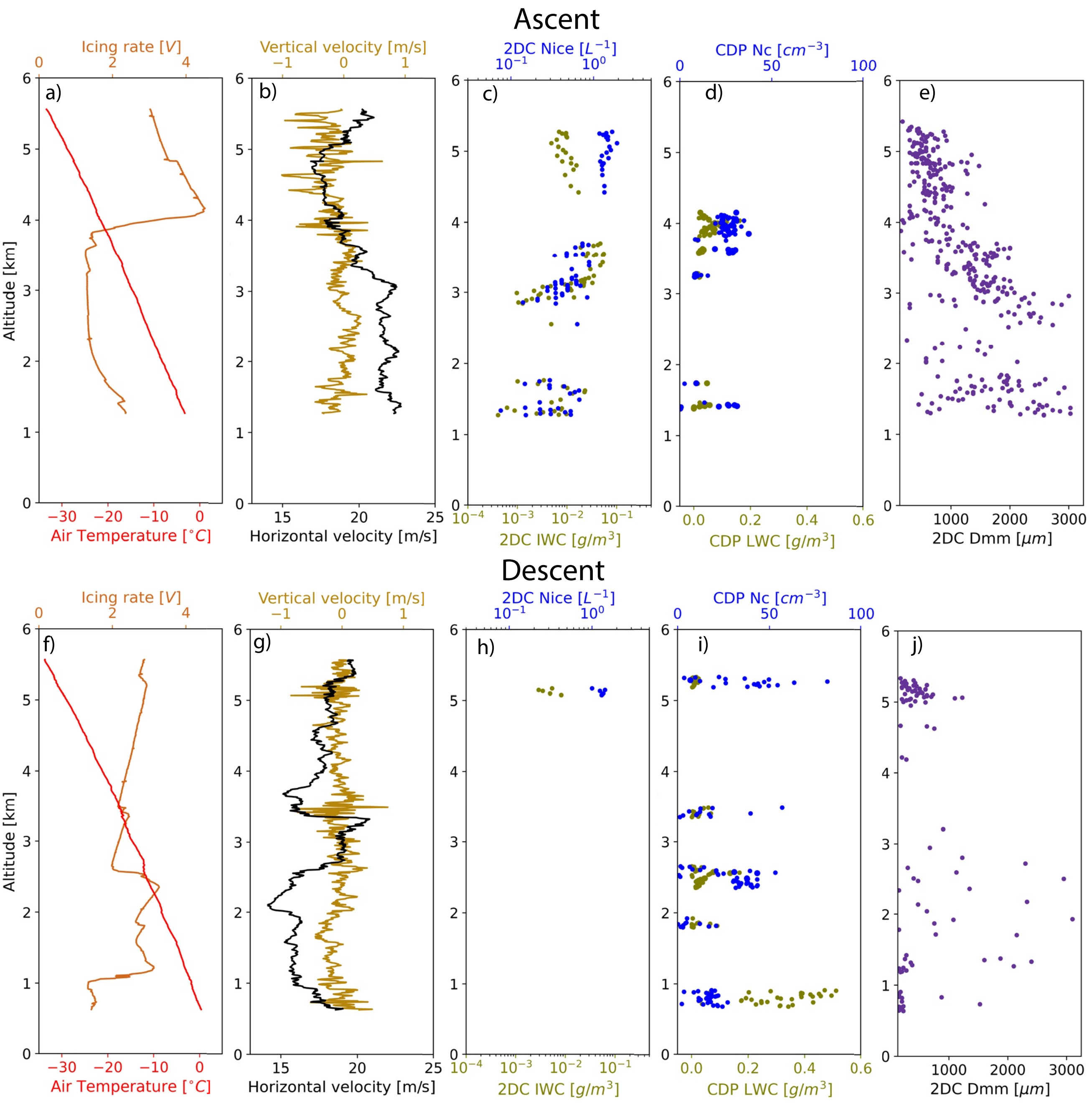

**Figure 9.** (a and f) Temperature (red) and Supercooled Liquid Water (SLW, brown) proxy. (b and g) Vertical (yellow) and horizontal (black) wind speed. (c and h) Two-Dimensional Cloud Probe (2DC) Ice number concentration (Nice, blue) and Ice Water Content (IWC, green) derived for ice phase clouds only, (d and i) Cloud Droplet Probe (CDP) droplet concentration (Nc, blue) and Liquid Water Content (LWC, green) for mixed and liquid phase clouds. (e and j) 2DC Median mass diameter (Dmm). For one ascending, descending leg during the Gulfstream V (GV) aircraft overflight from the Research Vessel (RV) Investigator. Only values where the total water content is >0.005 $g/m^{-3}$ are plotted.

Overall, despite the somewhat non-classic warm front that was encountered during the overflight, the coincident airborne and shipborne radar reflectivity CFAD/CFTD analyses are largely consistent with the composite results in Section 3 for the M4 cluster. Figures 9e, 9j, and 10 suggest large ice from the in-situ probes. Although near the aircraft the HIAPER cloud phase product does not indicate large ice particles; the limited in-situ cloud data also support our interpretations of the HIAPER CFAD/CFTD analysis and associated microphysical processes. More in-situ data is necessary to enhance the evaluation for other clusters.

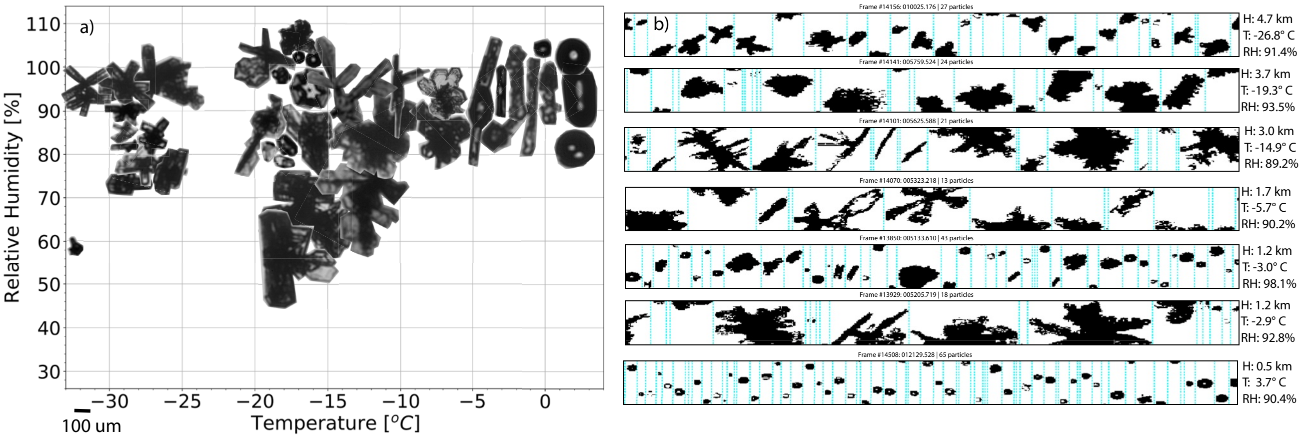

**Figure 10.** Particle images obtained by (a) the Particle Habit Imaging and Polar Scattering (PHIPS-HALO) stereo imaging instrument. Images are represented as a function of temperature and relative humidity. (b) The fast Two-Dimensional Cloud Probe probe. Both during the third flight of Southern Ocean Cloud Radiation and Aerosol Transport Experimental Study (RF03) in the vicinity of the Research Vessel Investigator (between 2018 and 01–23 00:20 to 01:29 UTC).

## 5. Conclusions and Discussion

Motivated by the need to better understand the Southern Ocean (SO) cloud and precipitation systems, this research capitalized on recent field observations from the CAPRICORN I and II) to examine the macro- and microphysical characteristics of the clouds and precipitation, under different thermodynamic and synoptic atmospheric conditions. Aircraft observations collected during research flight RF03 from the Southern Ocean Clouds Radiation Aerosol Transport Experimental Study (SOCRATES) were used to complement the analysis and to evaluate the interpretations of the shipborne remote-sensing information. It should be noted that the results presented here represent a qualitative description of the dominant cloud/precipitation features associated with different thermodynamic and synoptic conditions. In addition, the k-means clustering technique only represents conditions below 700 hPa level. More in-situ measurements under different synoptic conditions are needed to fully evaluate our interpretations.

To summarize, key findings of this study include:

1. Distinct cloud and precipitation regimes are found to correspond to the seven thermodynamic clusters established in Truong et al. (2020), over the Australian sector of the Southern Ocean. In contrast, cloud and precipitation regimes are less well defined using the cyclone and (cold) front compositing methods.
2. The warm front (M4) and the high-latitude cyclone (C1) clusters possess the highest fractions of surface precipitation, with the former being dominated by warm rain and the latter featuring the largest fraction of snow. Multiple lines of evidence suggest that ice aggregation in relatively deep convection likely dominates the particle growth in M4, while multiple microphysical mechanisms within cold clouds are present in C1.
3. The driest surface conditions are found to be associated with the Coastal Antarctica (C2) and high pressure (M1) clusters. Both represent a discontinuous dipole-like structure in the cloud vertical profiles, where low-level clouds are primarily non-precipitating.
4. The warm air advection cluster (W1) is characterized by a variety of cloud processes featuring a warm, deep, and moist troposphere. Unlike M4, only warm rain with a relatively weak intensity is recorded at the surface.
5. The cold frontal (M2) and post-frontal (M3) clusters feature similar surface precipitation characteristics. However, the M2 cluster represents a higher variability of ice processes and cloud types, while M3 has a high frequency of non-precipitating to lightly precipitating clouds (likely mixed phase) between −15 and 0°C.
6. The case study using in-situ observations from SOCRATES generally supports the interpretations made about the role of key microphysical processes using the cloud radar profiles. A variety of ice habits are observed across a wide range of temperatures down to −35°C under the M4 cluster.

The M3 cluster, which represents the cold sector of the cyclones over the midlatitude SO, is characterized by the predominance of shallow clouds (below 3 km and higher than −15°C) that are composed primarily of non-to weakly precipitating particles in the lower troposphere. These clouds have been reported to be most poorly simulated in weather and climate model at all scales, constituting a leading contributor to the previously noted shortwave radiative biases (Bodas-Salcedo et al., 2012, 2014, 2016). However, it is worth noting that recent research has documented the frequent presence of both the open and closed Mesoscale Cellular Convective (MCC) clouds in this environment (Lang et al., 2021, 2022), with contrasting cloud phase composition and precipitation rates (Ahn et al., 2017; Huang et al., 2017, 2021). Further analysis into the oceanic and atmospheric conditions would be necessary to refine our understanding of the associated cloud controlling factors. However, we hypothesize that common presence of non-to weakly precipitating closed MCC clouds should influence by permitting less incoming radiation to the surface.

The cloud and precipitation characteristics associated with the high-latitude cyclones (C1) are intriguing, as the geographical distribution of this cluster is spatially more correlated with the locations of the largest radiative biases in climate model simulations (Bodas-Salcedo et al., 2012). With the absence of warm clouds, ice (i.e., cold cloud) processes are expected to be dominant in this environment. Our analysis presents evidence of glaciation processes in these clouds, which are further supported by the largest fraction of snowfall recorded at the surface. This creates an open question as how to reconcile the prevailing argument on the lack of supercooled liquid water in climate models and the active glaciation evident in the ship observations over the high-latitude SO. Equally interesting is the Coastal Antarctica (C2) cluster which is strongly dominated by non-precipitating low clouds that are presumably mostly SLW, despite the precipitating clouds aloft. However, further in-situ data in C2 are needed to confirm the dominance of SLW. This is in sharp contrast to C1, and may be associated with the drying effect of the katabatic winds as discussed in Truong et al. (2020). Given that C2 cluster had much fewer soundings from the CAPRICORN experiments, additional data would be beneficial for a better characterization of this environment.

This study is the first, to our knowledge, to couple cloud and precipitation fields with the thermodynamic and synoptic conditions over the remote SO using newly available field observations. Our analysis shows that, to a large extent, clouds and the ensuant precipitation can be patterned by these atmospheric conditions. Leading microphysical processes are also inferred from the cloud radar reflectivites, Doppler velocity and temperature ranges; however, these interpretations should only be treated as a first-order, qualitative estimates that are in line with the given synoptic and thermodynamic conditions. Different ice habits are characterized by distinct falling speeds, which are difficult to distinguish using a single-frequency cloud radar. More in-situ data, together with innovative combinations of multiple remote-sensing observations, are needed to validate these interpretations. Future studies should also consider evaluating the realism of the identified relationships in model simulations, with the aid of instrument simulators.

Finally, while the cold-air sector of an extratropical cyclone possesses a large climatological-mean bias, the day-to-day processes governing how the clouds respond to dynamical perturbations are more flawed in the anticyclones and the frontal environments, as elaborated in a recent study where output from 10 models that participated in CMIP5 were analyzed (Kelleher & Grise, 2019). Here, our clustering framework would allow for a more direct identification of processes that may be inherently misrepresented in models.

**Acknowledgments**

This work is supported by the Australian Research Council discovery grant DP190101362. Y. Huang was also supported by the ARC Centre of Excellence for Climate Extremes (CE170100023). G.M. McFarquhar was supported by the National Science Foundation (NSF) through grants AGS-1628674 and AGS-1762096. The authors acknowledge the thorough work from the CAPRICORN and SOCRATES teams to collect, post-processing, and make available the data sets. The CAPRICORN data was collected using the RV Investigator, we thank the CSIRO Marine National Facility (MNF), the ship's personnel and the scientific team for the efforts made in gathering and post-processing the information. The SOCRATES data were collected using NSF's Lower Atmosphere Observing Facilities. The authors thank the pilots, mechanics, technicians, scientists, software engineers, and project managers of the NCAR EOL Research Aviation Facility for their support in the field and in post-processing data. The authors would like to thank the Australian Bureau of Meteorology Tasmanian regional Office for the forecast support and weather briefings provided during the field campaign with special thanks to Scott Carpentier, Michelle Hollister, Matthew Thomas, and Robert Schaap. We sincerely thank Son Truong for providing the cluster classification from CAPRICORN I and II field campaigns, Yang Wang and Julian Schima for giving access to processed data used in the construction of Figure 9. Open access publishing facilitated by The University of Melbourne, as part of the Wiley - The University of Melbourne agreement via the Council of Australian University Librarians.

## Data Availability Statement

The CAPRICORN I and II data used in the study are available at CSIRO via https://doi.org/10.25919/5f688fcc97166 with creative commons attribution 4.0 International. The SOCRATES data are managed and operated by NCAR's Earth Observing Laboratory, and are available at https://data.eol.ucar.edu/project/SOCRATES. All used data sets are available in the in-text data citation references: Schnaiter (2018), UCAR/NCAR EOL (2018a), UCAR/NCAR EOL (2018b), UCAR/NCAR EOL (2018c), UCAR/NCAR EOL (2019), Wu and McFarquhar (2019), and NCAR/EOL (2022).

## References

Abdelmonem, A., Järvinen, E., Duft, D., Hirst, E., Vogt, S., Leisner, T., & Schnaiter, M. (2016). Phips–Halo: The airborne particle habit imaging and polar scattering probe—Part 1: Design and operation. *Atmospheric Measurement Techniques*, *9*(7), 3131–3144. https://doi.org/10.5194/amt-9-3131-2016

Ahn, E., Huang, Y., Chubb, T. H., Baumgardner, D., Isaac, P., de Hoog, M., et al. (2017). In situ observations of wintertime low-altitude clouds over the southern ocean. *Quarterly Journal of the Royal Meteorological Society*, *143*(704), 1381–1394. https://doi.org/10.1002/qj.3011

Alexander, S. P., McFarquhar, G. M., Marchand, R., Protat, A., Vignon, E., Mace, G. G., & Klekociuk, A. R. (2021). Mixed-phase clouds and precipitation in southern ocean cyclones and cloud systems observed poleward of 64°S by ship-based cloud radar and lidar. *Journal of Geophysical Research: Atmospheres*, *126*(8). https://doi.org/10.1029/2020JD033626

Atlas, R. L., Bretherton, C. S., Blossey, P. N., Gettelman, A., Bardeen, C., Lin, P., & Ming, Y. (2020). How well do large-eddy simulations and global climate models represent observed boundary layer structures and low clouds over the summertime southern ocean? *Journal of Advances in Modeling Earth Systems*, *12*(11). https://doi.org/10.1029/2020MS002205

Bailey, M. P., & Hallet, J. (2009). A comprehensive habit diagram for atmospheric ice crystals: Confirmation from the laboratory, AIRS II, and other field studies. *Journal of the Atmospheric Sciences*, *66*(9), 2888–2899. https://doi.org/10.1175/2009JAS2883.1

Baker, B., & Lawson, R. P. (2006). Improvement in determination of ice water content from two-dimensional particle imagery. Part I: Image-to-mass relationships. *Journal of Applied Meteorology and Climatology*, *45*(9), 1282–1290. https://doi.org/10.1175/JAM2398.1

Baumgardner, D., Abel, S. J., Axisa, D., Cotton, R., Crosier, J., Field, P., et al. (2017). Cloud ice properties: In situ measurement challenges. *Meteorological Monographs*, *58*, 9.1–9.23. https://doi.org/10.1175/AMSMONOGRAPHS-D-16-0011.1

Baumgardner, D., & Rodi, A. (1989). Laboratory and wind tunnel evaluations of the rosemount icing detector. *Journal of Atmospheric and Oceanic Technology*, *6*, 971–979. https://doi.org/10.1175/1520-0426(1989)006<0971:lawteo>2.0.co;2

Berry, G., Reeder, M. J., & Jakob, C. (2011). A global climatology of atmospheric fronts. *Geophysical Research Letters*, *38*(4). https://doi.org/10.1029/2010GL046451

Bodas-Salcedo, A., Andrews, T., Karmalkar, A. V., & Ringer, M. A. (2016). Cloud liquid water path and radiative feedbacks over the southern ocean. *Geophysical Research Letters*, *43*(20), 10938–10946. https://doi.org/10.1002/2016GL070770

Bodas-Salcedo, A., Webb, M. J., Bony, S., Chepfer, H., Dufresne, J.-l., Klein, S. A., et al. (2011). COSP: Satellite simulation software for model assessment. *Bulletin of the American Meteorological Society*, *92*(8), 1023–1043. https://doi.org/10.1175/2011BAMS2856.1

Bodas-Salcedo, A., Williams, K. D., Field, P. R., & Lock, A. P. (2012). The surface downwelling solar radiation surplus over the southern ocean in the met office model: The role of midlatitude cyclone clouds. *Journal of Climate*, *25*(21), 7467–7486. https://doi.org/10.1175/JCLI-D-11-00702.1

Bodas-Salcedo, A., Williams, K. D., Ringer, M. A., Beau, I., Cole, J. N. S., Dufresne, J. L., et al. (2014). Origins of the solar radiation biases over the Southern Ocean in CFMIP2 models. *Journal of Climate*, *27*(1), 41–56. https://doi.org/10.1175/JCLI-D-13-00169.1

Ceppi, P., Zelinka, M. D., & Hartmann, D. L. (2016). The response of the southern hemispheric eddy-driven jet to future changes in shortwave radiation in CMIP5. *Geophysical Research Letters*, *41*(9), 3244–3250. https://doi.org/10.1002/2014GL060043

D'Alessandro, J. J., McFarquhar, G. M., Wu, W., Stith, J. L., Jensen, J. B., & Rauber, R. M. (2021). Characterizing the occurrence and spatial heterogeneity of liquid, ice, and mixed phase low-level clouds over the southern ocean using in situ observations acquired during socrates. *Journal of Geophysical Research: Atmospheres*, *126*(11). https://doi.org/10.1029/2020JD034482

Delanoë, J., Protat, A., Vinson, J., Brett, W., Caudoux, C., Bertrand, F., et al. (2016). BASTA: A 95-GHz FMCW Doppler radar for cloud and fog studies. *Journal of Atmospheric and Oceanic Technology*, *33*(5), 1023–1038. https://doi.org/10.1175/jtech-d-15-0104.1

Diao, M. (2018). Calibration of the vertical cavity surface emitting laser (VCSEL) water vapor hydrometer. *[Conference presentation]*. Retrieved from http://works.bepress.com/minghui-diao/50/

Dodson, J. B., Taylor, P. C., & Branson, M. (2018). Microphysical variability of Amazonian deep convective cores observed by cloudsat and simulated by a multi-scale modeling framework. *Atmospheric Chemistry and Physics*, *18*(9), 6493–6510. https://doi.org/10.5194/acp-18-6493-2018

Finlon, J. A., Rauber, R. M., Wu, W., Zaremba, T. J., McFarquhar, G. M., Nesbitt, S. W., et al. (2020). Structure of an atmospheric river over Australia and the Southern Ocean: II. Microphysical evolution. *Journal of Geophysical Research: Atmospheres*, *125*(18). https://doi.org/10.1029/2020JD032514

Foote, G. B., & Du Toit, P. S. (1969). Terminal velocity of raindrops aloft. *Journal of Applied Meteorology and Climatology*, *8*(2), 249–253. https://doi.org/10.1175/1520-0450(1969)008<0249:tvora>2.0.co;2

Franklin, C. N., Sun, Z., Bi, D., Dix, M., Yan, H., & Bodas-Salcedo, A. (2013). Evaluation of clouds in access using the satellite simulator package COSP: Regime-sorted tropical cloud properties. *Journal of Geophysical Research: Atmospheres*, *118*(12), 6663–6679. https://doi.org/10.1002/jgrd.50496

Gettelman, A., Bardeen, C. G., McCluskey, C., Järvinen, E. J., Stith, J., Bretherton, C., et al. (2020). Simulating observations of Southern Ocean clouds and implications for climate. *Journal of Geophysical Research: Atmospheres*, *125*(21). https://doi.org/10.1029/2020JD032619

Gettelman, A., Hannay, C., Bacmeister, J. T., Neale, R. B., Pendergrass, A. G., Danabasoglu, G., et al. (2019). High climate sensitivity in the community Earth system model version 2 (CESM2). *Geophysical Research Letters*, *46*(14), 8329–8337. https://doi.org/10.1029/2019GL083978

Haynes, J. M., L'Ecuyer, T. S., Stephens, G. L., Miller, S. D., Mitrescu, C., Wood, N. B., & Tanelli, S. (2009). Rainfall retrieval over the ocean with spaceborne w-band radar. *Journal of Geophysical Research*, *114*, D00A22. https://doi.org/10.1029/2008JD009973

Huang, Y., Chubb, T., Baumgardner, D., de Hoog, M., Siems, S. T., & Manton, M. J. (2017). Evidence for secondary ice production in Southern Ocean open cellular convection. *Quarterly Journal of the Royal Meteorological Society*, *143*(704), 1685–1703. https://doi.org/10.1002/qj.3041

Huang, Y., Protat, A., Siems, S. T., & Manton, M. J. (2015). A-train observations of maritime midlatitude storm-track cloud systems: Comparing the Southern Ocean against the North Atlantic. *Journal of Climate*, *28*(5), 1920–1939. https://doi.org/10.1175/JCLI-D-14-00169.1

Huang, Y., Siems, S. T., & Manton, M. J. (2021). Wintertime in situ cloud microphysical properties of mixed-phase clouds over the southern ocean. *Journal of Geophysical Research: Atmospheres*, *126*(11). https://doi.org/10.1029/2021JD034832

Huang, Y., Siems, S. T., Manton, M. J., Protat, A., Majewski, L., & Nguyen, H. (2019). Evaluating Himawari-8 cloud products using shipborne and CALIPSO observations: Cloud-top height and cloud-top temperature. *Journal of Atmospheric and Oceanic Technology*, *36*(12), 2327–2347. https://doi.org/10.1175/JTECH-D-18-0231.1

Järvinen, E., McCluskey, C. S., Waitz, F., Schnaiter, M., Bansemer, A., Bardeen, C. G., et al. (2022). Evidence for Secondary Ice Production in Southern Ocean Maritime Boundary Layer Clouds. *Journal of Geophysical Research: Atmospheres*, *127*, e2021JD036411. https://doi.org/10.1029/2021JD036411

Kay, J. E., Wall, C., Yettella, V., Medeiros, B., Hannay, C., Caldwell, P., & Bitz, C. (2016). Global climate impacts of fixing the Southern Ocean shortwave radiation bias in the community Earth system model (CESM). *Journal of Climate*, *29*(12), 4617–4636. https://doi.org/10.1175/JCLI-D-15-0358.1

Kelleher, M. K., & Grise, K. M. (2019). Examining southern ocean cloud controlling factors on daily time scales and their connections to midlatitude weather systems. *Journal of Climate*, *32*(16), 5145–5160. https://doi.org/10.1175/JCLI-D-18-0840.1

Kikuchi, K., Kameda, T., Higuchi, K., & Yamashita, A. (2013). A global classification of snow crystals, ice crystals, and solid precipitation based on observations from middle latitudes to polar regions. *Atmospheric Research*, 132–133. https://doi.org/10.1016/j.atmosres.2013.06.006

Klepp, C., Michel, S., Protat, A., Burdanowitz, J., Albern, N., Kähnert, M., et al. (2018). OceanRAIN, a new in-situ shipboard global ocean surface-reference dataset of all water cycle components. *Scientific Data*, *5*(1), 180122. https://doi.org/10.1038/sdata.2018.122

Lance, S., Brock, C. A., Rogers, D., & Gordon, J. A. (2010). Water droplet calibration of the cloud droplet probe (CDP) and in-flight performance in liquid, ice and mixed-phase clouds during arcpac. *Atmospheric Measurement Techniques*, *3*(6), 1683–1706. https://doi.org/10.5194/amt-3-1683-2010

Lang, F., Ackermann, L., Huang, Y., Truong, S. C. H., Siems, S. T., & Manton, M. J. (2022). A climatology of open and closed mesoscale cellular convection over the southern ocean derived from Himawari-8 observations. *Atmospheric Chemistry and Physics*, *22*(3), 2135–2152. https://doi.org/10.5194/acp-22-2135-2022

Lang, F., Huang, Y., Protat, A., Truong, S. C. H., Siems, S. T., & Manton, M. J. (2021). Shallow convection and precipitation over the southern ocean: A case study during the Capricorn 2016 field campaign. *Journal of Geophysical Research: Atmospheres*, *126*(9). https://doi.org/10.1029/2020JD034088

Lang, F., Huang, Y., Siems, S., & Manton, M. (2018). Characteristics of the marine atmospheric boundary layer over the Southern Ocean in response to the synoptic forcing. *Journal of Geophysical Research: Atmospheres*, *123*. https://doi.org/10.1029/2018JD028700

Lang, F., Huang, Y., Siems, S. T., & Manton, M. J. (2020). Evidence of a diurnal cycle in precipitation over the Southern Ocean as observed at Macquarie Island. *Atmosphere*, *11*(2), 181. https://doi.org/10.3390/atmos11020181

Mace, G. G., & Protat, A. (2018a). Clouds over the Southern Ocean as observed from the R/V investigator during CAPRICORN. Part I: Cloud occurrence and phase partitioning. *Journal of Applied Meteorology and Climatology*, *57*(8), 1783–1803. https://doi.org/10.1175/JAMC-D-17-0194.1

Mace, G. G., & Protat, A. (2018b). Clouds over the Southern Ocean as observed from the R/V investigator during CAPRICORN. Part II: The properties of nonprecipitating stratocumulus. *Journal of Applied Meteorology and Climatology*, *57*(8), 1805–1823. https://doi.org/10.1175/JAMC-D-17-0195.1

Mace, G. G., Protat, A., Humphries, R. S., Alexander, S. P., McRobert, I. M., Ward, J., et al. (2021). Southern Ocean cloud properties derived from CAPRICORN and MARCUS data. *Journal of Geophysical Research: Atmospheres*, *125*(4). https://doi.org/10.1029/2020JD033368

Marchand, R., Wood, R., Bretherton, C., McFarquhar, G. M., Protat, A., Quinn, P., et al. (2014). The Southern Ocean Clouds, Radiation, Aerosol transport Experimental Study (SOCRATES). In Workshop on clouds, aerosols, radiation and air-sea interface of the southern ocean. *Establishing Directions For Future Research*.

Mason, S., Fletcher, J. K., Haynes, J. M., Franklin, C., Protat, A., & Jakob, C. (2015). A hybrid cloud regime methodology used to evaluate Southern Ocean cloud and shortwave radiation errors in ACCESS. *Journal of Climate*, *28*(15), 6001–6018. https://doi.org/10.1175/JCLI-D-14-00846.1

McCoy, I. L., Bretherton, C. S., Wood, R., Twohy, C. H., Gettelman, A., Bardeen, C. G., & Toohey, D. W. (2021). Influences of recent particle formation on southern ocean aerosol variability and low cloud properties. *Journal of Geophysical Research: Atmospheres*, *126*(8). https://doi.org/10.1029/2020JD033529

McFarquhar, G. M., Baumgardner, D., Bansemer, A., Abel, S. J., Crosier, J., French, J., et al. (2017). Processing of ice cloud in situ data collected by bulk water, scattering, and imaging probes: Fundamentals, uncertainties, and efforts toward consistency. *Meteorological Monographs*, *58*, 11.1–11.33. https://doi.org/10.1175/AMSMONOGRAPHS-D-16-0007.1

McFarquhar, G. M., Bretherton, C., Marchand, R., Protat, A., DeMott, P. J., Alexander, S. P., et al. (2021). Observations of clouds, aerosols, precipitation, and surface radiation over the Southern Ocean: An overview of CAPRICORN, MARCUS, MICRE, and SOCRATES. *Bulletin of the American Meteorological Society*, *102*(4), E894–E928. https://doi.org/10.1175/BAMS-D-20-0132.1

McFarquhar, G. M., Finlon, J. A., Stechman, D. M., Wu, W., Jackson, R. C., & Freer, M. (2018). University of Illinois/Oklahoma optical Array probe (OAP) processing software [Software]. Zenodo. https://doi.org/10.5281/zenodo.1285969

McFarquhar, G. M., Um, J., & Jackson, R. (2013). Small cloud particle shapes in mixed-phase clouds. *Journal of Applied Meteorology and Climatology*, *52*(5), 1277–1293. https://doi.org/10.1175/JAMC-D-12-0114.1

Mitchell, D. L. (1996). Use of mass- and area-dimensional power laws for determining precipitation particle terminal velocities. *Journal of the Atmospheric Sciences*, *53*(12), 1710–1723. https://doi.org/10.1175/1520-0469(1996)053<1710:uomaad>2.0.co;2

Mülmenstädt, J., Salzmann, M., Kay, J., Zelinka, M., Ma, P., Nam, C., et al. (2021). An underestimated negative cloud feedback from cloud lifetime changes. *Nature Climate Change*, *11*(6), 508–513. https://doi.org/10.1038/s41558-021-01038-1

Murray, R. J., & Simmonds, I. (1991). A numerical scheme for tracking cyclone centres from digital data. Part I: Development and operation of the scheme. *Australian Meterological Magazine*, *39*.

Naud, C. M., Booth, J. F., & Del Genio, A. D. (2014). Evaluation of ERA-interim and MERRA cloudiness in the Southern Ocean. *Journal of Climate*, *27*(5), 2109–2124. https://doi.org/10.1175/JCLI-D-13-00432.1

NCAR/EOL. (2022). Ncar hcr radar and hsrl lidar moments data. version 3.0 [Dataset]. https://doi.org/10.5065/D68914PH

Pepler, A. S., Dowdy, A. J., van Rensch, P., Rudeva, I., Catto, J. L., & Hope, P. (2020). The contributions of fronts, lows and thunderstorms to southern Australian rainfall. *Climate Dynamics*, *55*(5–6), 1489–1505. https://doi.org/10.1007/s00382-020-05338-8

Protat, A., Schulz, E., Rikus, L., Sun, Z., Xiao, Y., & Keywood, M. (2017). Shipborne observations of the radiative effect of Southern Ocean clouds. *Journal of Geophysical Research: Atmospheres*, *122*(1), 318–328. https://doi.org/10.1002/2016JD026061

Romatschke, U., & Vivekanandan, J. (2022). Cloud and precipitation particle identification using cloud radar and lidar measurements: Retrieval technique and validation. *Earth and Space Science*, *9*(5). https://doi.org/10.1029/2022EA002299

Schima, J., McFarquhar, G., Romatschke, U., Vivekanandan, J., D'Alessandro, J., Haggerty, J., et al. (2022). Characterization of southern ocean boundary layer clouds using airborne radar, lidar, and in-situ cloud data: Results from socrates. Retrieved from https://agu.confex.com/agu/fm21/meetingapp.cgi/Paper/980227

Schnaiter, M. (2018). Phips-halo stereo imaging data. Version 1.0 [Dataset]. https://doi.org/10.5065/D62B8WWF

Schnaiter, M., Järvinen, E., Abdelmonem, A., & Leisner, T. (2018). Phips-halo: The airborne particle habit imaging and polar scattering probe. Part 2: Characterization and first results. *Atmospheric Measurement Techniques*, *11*(1), 341–357. https://doi.org/10.5194/amt-11-341-2018

Thompson, G., Field, P. R., Rasmussen, R. M., & Hall, W. D. (2008). Explicit forecasts of winter precipitation using an improved bulk microphysics scheme. Part II: Implementation of a new snow parameterization. *Monthly Weather Review*, *136*(12), 5095–5115. https://doi.org/10.1175/2008MWR2387.1

Truong, S., Huang, Y., Land, F., Messmer, M., Simmonds, I., Siems, S., & Manton, M. (2020). A climatology of the marine atmospheric boundary layer over the Southern Ocean from four field campaigns during 2016–2018. *Journal of Geophysical Research: Atmospheres*, *125*(20). https://doi.org/10.1029/2020JD033214

UCAR/NCAR, EOL. (2014). Hiaper cloud radar (HCR). (Tech. Rep). https://doi.org/10.5065/D6BP00TP

UCAR/NCAR EOL. (2018a). Capricorn r/v investigator 95-ghz Doppler cloud radar (basta) level 2 data [Dataset]. Retrieved from https://data.eol.ucar.edu/dataset/552.038

UCAR/NCAR EOL. (2018b). Ncar/eol iss radiosonde data. Version 1.0 [Dataset]. https://doi.org/10.5065/D69P30HG

UCAR/NCAR, EOL. (2018c). NCAR/EOL quality controlled dropsonde data. version 1.1 [Dataset]. https://doi.org/10.5065/D6QZ28SG

UCAR/NCAR, EOL. (2019). Socrates: Low rate (LRT—1 SPS) navigation, state parameter, and microphysics flight-level data. Version 1.3 [Dataset]. Donee. https://doi.org/10.5065/D6M32TM9

Vivekanandan, J., Ellis, S., Tsai, P., Loew, E., Lee, W.-C., Emmett, J., et al. (2015). A wing pod-based millimeter wavelength airborne cloud radar. *Geoscientific Instrumentation, Methods and Data Systems*, *4*(2), 161–176. https://doi.org/10.5194/gi-4-161-2015

Wang, Y., McFarquhar, G. M., Rauber, R. M., Zhao, G., Wu, W., Finlon, J. A., et al. (2020). Microphysical properties of generating cells over the Southern Ocean: Results from SOCRATES. *Journal of Geophysical Research: Atmospheres*, *125*(13). https://doi.org/10.1029/2019JD032237

Wang, Y., Zhao, C., McFarquhar, G. M., Wu, W., Reeves, M., & Li, J. (2021). Dispersion of droplet size distributions in supercooled non-precipitating stratocumulus from aircraft observations obtained during the southern ocean cloud radiation aerosol transport experimental study. *Journal of Geophysical Research: Atmospheres*, *126*(6). https://doi.org/10.1029/2020JD033720

Wang, Z., Siems, S. T., Belusic, D., Manton, M. J., & Huang, Y. (2015). A climatology of the precipitation over the southern ocean as observed at Macquarie Island. *Journal of Applied Meteorology and Climatology*, *54*(12), 2321–2337. https://doi.org/10.1175/jamc-d-14-0211.1

Williams, K., Bodas-Salcedo, A., Déqué, M., Fermepin, S., Medeiros, B., Jakob, C., et al. (2013). The transpose-AMIP II experiment and its application to the understanding of Southern Ocean cloud biases in climate models. *Journal of Cimate*, *26*(10), 3258–3274. https://doi.org/10.1175/JCLI-D-12-00429.1

Wood, R., Kubar, T. L., & Hartmann, D. L. (2009). Understanding the importance of microphysics and macrophysics for warm rain in marine low clouds. Part II: Heuristic models of rain formation. *Journal of the Atmospheric Sciences*, *66*(10), 2973–2990. https://doi.org/10.1175/2009JAS3072.1

Wu, W., & McFarquhar, G. M. (2016). On the impacts of different definitions of maximum dimension for nonspherical particles recorded by 2D imaging probes. *Journal of Atmospheric and Oceanic Technology*, *33*(5), 1057–1072. https://doi.org/10.1175/JTECH-D-15-0177.1

Wu, W., & McFarquhar, G. M. (2019). Sf/ncar gv hiaper fast 2dc particle size distribution (PSD) product data. Version 1.1 [Dataset]. https://doi.org/10.26023/E95A-FKYF-7P0R

Yuter, S. E., & Houze, R. A. J. (1995). Three-dimensional kinematic and microphysical evolution of Florida cumulonimbus. Part II: Frequency distributions of vertical velocity, reflectivity, and differential reflectivity. *Monthly Weather Review*, *123*(7), 1941–1963. https://doi.org/10.1175/1520-0493(1995)123<1941:tdkame>2.0.co;2

Zaremba, T. J., Rauber, R. M., McFarquhar, G. M., Hayman, M., Finlon, J. A., & Stechman, D. M. (2020). Phase characterization of cold sector Southern Ocean cloud tops: Results from SOCRATES. *Journal of Geophysical Research: Atmospheres*, *125*(24). https://doi.org/10.1029/2020JD033673

Zelinka, M. D., Myers, T. A., McCoy, D. T., Po-Chedley, S., Caldwell, P. M., Ceppi, P., et al. (2020). Causes of higher climate sensitivity in CMIP6 models. *Geophysical Research Letters*, *47*(1). https://doi.org/10.1029/2019GL085782

Zhao, X., Liu, X., Burrows, S. M., & Shi, Y. (2021). Effects of marine organic aerosols as sources of immersion-mode ice-nucleating particles on high-latitude mixed-phase clouds. *Atmospheric Chemistry and Physics*, *21*(4), 2305–2327. https://doi.org/10.5194/acp-21-2305-2021

Zhou, X. R. A. L. M. I., Bretherton, C. S., Bardeen, C., Gettelman, A., & Ming, Y. (2020). Evaluation of cloud and precipitation simulations in CAM6 and AM4 using observations over the Southern Ocean. *Earth and Space. Earth and Space Science*, *8*(2). https://doi.org/10.1029/2020EA001241